Hydrothermal solubility of $TbPO_4$, $HoPO_4$, $TmPO_4$, and $LuPO_4$ xenotime endmembers at pH of 2 and temperatures between 100 and 250 °C

Alexander P. Gysi[a,b,c,*], Christopher Van Hoozen[c], Daniel Harlov[d,e,f]

[a] *New Mexico Bureau of Geology and Mineral Resources, New Mexico Institute of Mining and Technology, Socorro, NM 87801, USA*
[b] *Department of Earth and Environmental Science, New Mexico Institute of Mining and Technology, Socorro, NM 87801, USA*
[c] *Center for Mineral Resources Science, Department of Geology and Geological Engineering, Colorado School of Mines, Golden, CO 80401, USA*
[d] *GeoforschungsZentrum, Telegrafenberg, D-14473 Potsdam, Germany*
[e] *Department of Geology, University of Johannesburg P.O. Box 524, Auckland Park, 2006*
[f] *State Key Laboratory of Geological Processes and Mineral Resources, China University of Geosciences, Wuhan 430074, China*

Abstract

Rare earth element (REE) phosphates such as xenotime (YPO_4) are important hosts to the heavy (H)REE in natural systems. Xenotime is commonly associated with hydrothermal alteration and mineral replacement reactions and its composition may yield important clues about the mineralization processes from aqueous fluids in REE mineral deposits. Robust underlying thermodynamic data for the REE phosphate endmembers and aqueous species are required to simulate the stability of xenotime and the mobility of REE in natural hydrothermal fluids. In this study, the solubility of synthetic $TbPO_4$, $HoPO_4$, $TmPO_4$, and $LuPO_4$ endmembers has been measured in aqueous solutions between 100 and 250 °C at saturated water vapor pressure. The

---

[*] Corresponding author

Email address: `Alexander.Gysi@nmt.edu` (Alexander P. Gysi)

solubility products (K_{s0}) determined in the experiments were compared to values retrieved from a combination of calorimetric data for the REE phosphates and thermodynamic properties of the aqueous REE species at elevated temperatures. The solubility of xenotime is retrograde and generally higher in the experiments than predicted by different sources of thermodynamic data. To resolve these discrepancies, the solubility data were used to optimize the thermodynamic properties of the REE phosphate endmembers and REE aqueous species. These optimizations permit retrieving a set of provisional standard Gibbs energy of formation for REE^{3+} and $REEOH^{2+}$ at elevated temperature and were used to derive the following updated K_{s0} values (uncertainty of ± 0.2 at the 95% confidence) for the reaction $REEPO_4(s) = REE^{3+} + PO_4^{3-}$:

t (°C)	logK_{s0}($TbPO_4$)	logK_{s0}($HoPO_4$)	logK_{s0}($TmPO_4$)	logK_{s0} ($LuPO_4$)
100	-27.3	-27.7	-27.9	-28.1
150	-28.8	-29.2	-29.5	-29.6
200	-30.6	-30.9	-31.2	-31.4
250	-32.7	-32.9	-33.3	-33.4

The updated thermodynamic data generated from the solubility experiments have a significant impact on simulated xenotime compositions and predicted mobility of REE in crustal fluids. Future efforts are necessary to better constrain the properties of REE hydroxyl species at elevated temperature and possible non-ideal solid solution behavior for REE with ionic sizes significantly different from Y^{3+}.

Keywords: Solubility experiments, rare earth elements (REE), xenotime, critical minerals, thermodynamics

---

1. Introduction

Xenotime (YPO_4) is an accessory mineral that has been used together with monazite ($CePO_4$) as a U−Pb geochronometer and geothermometer to unravel the evolution of igneous, metamorphic and sedimentary rocks in different geologic settings (Gratz and Heinrich, 1997, 1998; Heinrich et al., 1997; Andrehs and Heinrich, 1998; Poitrasson et al., 2002; Hetherington et al., 2008). For example, hydrothermal xenotime overgrowths on detrital zircon grains were used to constrain the diagenetic evolution of the Archean Witwatersrand Supergroup of South Africa (England et al., 2002). In situ U−Pb dating of monazite and xenotime inclusions in 4.25−3.35 Ga detrital zircon from Jack Hills in Australia was used to reconstruct the post-depositional metasomatic and metamorphic history of Hadean age zircon at temperatures between 350 and 475 °C (Rasmussen et al., 2011). In the Browns Range in Australia, xenotime was found to have formed at temperatures between 100 and 120 °C in hydrothermal veins within a sedimentary basin (Cook et al., 2013; Richter et al., 2018). In iron-oxide-apatite (IOA) deposits, hydrothermal xenotime and monazite commonly grow from fluorapatite during metasomatism such as observed in the Pea Ridge deposit in Missouri (Harlov et al., 2016). Therefore, the chemistry of xenotime has potential for tracing hydrothermal processes in these different geologic environments over a wide range of temperatures.

Only a few hydrothermal solubility experiments have been undertaken that permit deriving the solubility products (K_{s0}) for a few xenotime endmembers. The solubility of YPO_4 was measured at pH $\leq$2 and at 23 and 50 °C in the study by Cetiner et al. (2005), and the solubility of YPO_4,

$DyPO_4$, $ErPO_4$, and $YbPO_4$ was measured at pH of 2 between 100 and 250 °C in the study by Gysi et al. (2015). Both of these studies indicate that the REE phosphates with the xenotime structure have very low and retrograde solubilities between 25 – 250 °C. Gysi et al. (2015) reports total dissolved Y concentrations of 1×10^{-7} to 1×10^{-8} m between 100 – 250 °C, whereas Cetiner et al. (2005) reports Y concentrations of 1×10^{-4} to 1×10^{-6} m between 23 – 50 °C. Comparison to other xenotime solubility experiments is difficult because previous work focused mostly on close to ambient temperature solubility measurements of hydrated REE phosphates (Jonasson et al., 1985; Byrne and Kim, 1993; Liu and Byrne, 1997; Gausse et al., 2016). These hydrated phases have higher reported solubilities than either monazite or xenotime, and are metastable phosphates at $<$100 °C (Du Fou de Kerdaniel et al., 2007; Gysi et al., 2015; Gausse et al., 2016; Arinicheva et al., 2018; Gysi et al., 2018). Other experiment were carried out at pressures ($\geq$0.5 GPa) and temperatures relevant to high-grade metamorphism (Tropper et al., 2011, 2013; Tanis et al., 2012; Zhou et al., 2016; Mair et al., 2017) at which the determination of solubility products is challenging.

Louvel et al. (2015) studied the solubility of $YbPO_4$ and speciation of Yb up to 400 °C and 50 MPa in 0.35 – 0.75 m HCl-bearing solutions using *in situ* X-ray absorption measurements. Their study reports a retrograde $YbPO_4$ solubility between 25 – 400 °C and Yb concentrations ranging from 1×10^{-3} to 1×10^{-4} m controlled by the formation of the hydrated REE^{3+} ion and chloro-aqua complexes at acidic pH values (Louvel et al., 2015). In the xenotime solubility study by Gysi et al. (2015), lower Yb concentrations of 1×10^{-7} to 1×10^{-10} m are reported between 100 – 250 °C at a pH of 2 in $HClO_4$-H_3PO_4 based aqueous solutions. In the presence of Cl^-, the REE solubility is expected to be controlled by REE chloride complexes (Migdisov et al., 2016), whereas the REE^{3+} ion is generally the dominant aqueous REE species in perchlorate based ($ClO_4{}^-$) acidic experimental solutions (Gysi et al., 2015; Van Hoozen et al., 2020). Several hydrothermal monazite solubility experiments also indicate that REE hydroxyl complexes may contribute to the measured REE solubility in acidic aqueous solutions (Pourtier et al., 2010; Gysi et al., 2018; Van Hoozen et al., 2020). However, the thermodynamic properties of REE hydroxyl complexes are not well known above 100 °C (Migdisov et al., 2016) and speciation calculations rely on theoretical extrapolations such as those by Haas et al. (1995).

Here we present hydrothermal experiments between 100 and 250 °C at saturated water vapor pressure and measured the solubility of synthetic $TbPO_4$, $HoPO_4$, $TmPO_4$, and $LuPO_4$ endmembers in perchloric acid based aqueous solutions. These solubility data are compared to available thermodynamic data for the HREE phosphate endmembers and aqueous REE species. This study permits critically assessing the cause of observed discrepancies between the solubility measurements and a combination of thermodynamic data from minerals and aqueous species from different sources.

2. Methods

2.1. Experimental

The hydrothermal solubility experiments were carried out using a similar method as previously developed for the other REE phosphate endmembers (Gysi et al., 2015, 2018). Pure mm-sized euhedral crystals of $TbPO_4$,

$HoPO_4$, $TmPO_4$, and $LuPO_4$ with the tetragonal xenotime structure were synthesized using the Na_2CO_3/MoO_3 flux method of Cherniak et al. (2004). Scanning electron microscopy images (Electronic Annex) show the morphology of unreacted and reacted crystal surfaces. The recourse to mm-sized synthetic xenotime crystals and the limitation of experiments to temperatures $\geq$ 100 °C enables overcoming issues associated with the precipitation of metastable hydrated REE phosphates at lower temperatures (Gausse et al., 2016; Arinicheva et al., 2018; Gysi et al., 2018) and the highly variable equilibriation times of synthetic REE phosphate powders (Liu and Byrne, 1997).

Each of these synthetic crystals was mounted in a titanium sample holder (Ti-foil with 99.7 % purity; Alfa Aesar) and placed in separate 45 ml teflon-lined stainless-steel autoclaves (Parr 4744), which were then filled with 25 ml of the starting aqueous solutions to cover the sample holders. The experimental starting solutions were prepared using trace metal grade (Fischer Scientific) perchloric acid ($HClO_4$) and milli-Q water (18 MΩ·s). A pH of 2.00 ±0.02 was measured at ambient temperature (22 ±2 °C). These pH measurements were used to determine the perchloric acid concentration in the starting solutions. This pH was selected to increase sufficiently the solubility of the REE phosphates and $HClO_4$ was used to avoid complexation from any additional ligands with REE^{3+} (Migdisov et al., 2016), therefore constraining the major species to REE^{3+} and $REEOH^{2+}$ depending on the temperature of the experiment (Gysi et al., 2018). These solutions were subsequently spiked with ~100 μl of a P-stock solution prepared from trace element grade (Fischer Scientific) phosphoric (H_3PO_4) acid. The headspace of each of the autoclaves containing the crystals and the starting solutions were purged with dry nitrogen, then sealed and the autoclaves placed in a muffle furnace (Cole-Parmer, EW-33858-70) at 100, 150, 200, and 250 °C for up to 16 days. Kinetic experiments were also conducted after different time intervals to verify approach to equilibrium. Temperature was recorded at the center of the furnace using an Omega® temperature logger with K-type thermocouples to ensure temperature was maintained within 0.5 °C.

At the end of each experiment, the autoclaves were quenched in a cold water bath for less than 20 minutes. The autoclaves were then opened and the reacted solutions pipetted out and diluted 1/6 with a 2 % nitric (HNO_3) acid blank matrix solution for the analysis of the P and REE concentrations using solution inductively coupled plasma mass spectrometry (ICP-MS). The sample holders were then removed, and the autoclave walls were washed. In-between experiments, a sulfuric acid wash was used to rinse the walls of the teflon liner of the autoclaves and the solutions further diluted with milliQ water for REE analysis using ICP-MS. None of these solutions showed any evidence for the formation of potential precipitates upon quenching of the experiments. These tests are also consistent with the absence of any other secondary phases on the reacted crystal surfaces (Electronic Annex). This behavior is expected since equilibrium was approached from undersaturation with very low REE concentrations in the reacted aqueous solutions (Table A.1). In between experimental runs, the teflon liners and sample holders were washed and soaked in concentrated sulfuric acid, followed by a day soaking in milli-Q water and rinsing.

2.2. Analytical

The pH of the starting experimental solutions was measured at room temperature using a Metrohm 913 pH meter (precision of ±0.003 pH units and resolution of 0.001 pH units) and a combined pH electrode (60260010 unitrode, Metrohm) with integrated Pt1000 temperature sensor. The electrode was calibrated using commercial buffer solutions from Fisher Scientific (pH of 2, 4, and 7; accuracy of ±0.01); pH-temperature compensated reading for the buffer solutions are considered by the built-in temperature sensor of the electrode to measure deviations from 25 °C. The ionic strengths of the experimental starting solutions (0.01 m) and the buffer solutions used for pH calibration (0.05 m) are relatively dilute; minor deviations are expected in the measured pH as a result of variations in liquid junction potentials. The estimated accuracy of pH measurements for the perchloric acid buffered starting experimental solutions is within ±0.03 pH units.

The quenched experimental solutions were analyzed for REE and P using a Perkin Elmer NexION 300Q quadrupole ICP-MS. Samples and standards were diluted using a 2 % HNO_3 blank matrix and spiked with In (SCP Science, NIST traceable) as an internal standard for drift corrections. Calibrations of ICP-MS analyses were carried out using a multi-element REE standard and two single REE standards (La and Ce; SCP Science, NIST traceable) for interference corrections due to oxide formation (Aries et al., 2000). Analyzed samples were blank-subtracted after drift correction. Phosphorus displays interference with nitrogen ($^{14}N^{16}OH$ and $^{15}N^{16}O$) from the 2 % HNO_3 blank matrix resulting in high background counts. Since the experimental starting solutions were spiked with P, the diluted quenched experimental solutions had concentrations well above the background of the blank (Table A.1), i.e. counts were 2−3 higher than the blank.

The analytical precision based on duplicate ICP-MS runs of standards was $\leq$3 % for P and $\leq$1.5 % for Tb, Ho, Tm, and Lu. The limit of detection (LOD) was determined by multiple measurements of the blank using the 3 σ (standard deviation of the mean) values. The determined LOD values were 10 ppb for P, and between 10 and 100 ppt for the REE.

2.3. Aqueous speciation calculations

Aqueous speciation and ion activities were calculated using the GEMS code package version 3.5 (Kulik et al., 2013) combined with the TSolmod library containing the relevant activity models and equations-of-state (Wagner et al., 2012). The thermodynamic properties of the aqueous species were retrieved at temperature and pressure of interest using the Helgeson-Kirkham-Flowers (HKF) equation-of-state (Helgeson et al., 1981; Shock and Helgeson, 1988; Tanger and Helgeson, 1988; Shock et al., 1992). These data for aqueous species are collectively referred here to "Supcrt92" from the slop98.dat database originally implemented in the SUPCRT92 computer code by Johnson et al. (1992). The properties of water were calculated from the IAPS-84 equation-of-state (Kestin et al., 1984). The thermodynamic data and aqueous species considered in the speciation calculations are listed in Table 1.

The activities of the aqueous species of interest were determined at the experimental temperatures and pressures from the measured REE and P concentrations of the quenched experimental solutions (Table A.1). The activity coefficients (γ_i) of charged aqueous species were calculated using the extended Debye-Hückel equation (Robinson and Stokes, 1968):

$$\log \gamma_i = -\frac{A z_i^2}{1 + \mathring{a}_i B} + \Gamma_\gamma + b_\gamma I \tag{1}$$

and the ionic strength (I) is given by,

$$I = 1/2 \sum m_i z_i^2 \tag{2}$$

A and B are the Debye-Hückel parameters (Helgeson et al., 1981); Γ_γ is a mole fraction to molality conversion factor; b_γ is the extended term parameter, which has a value of 0.21 for $HClO_4/NaClO_4$ aqueous solutions up to 250 °C (Migdisov and Williams-Jones, 2007); $\mathring{a}_i$ is the ion size parameter taken from Migdisov and Williams-Jones (2007) for ClO_4^- (4.5 Å) and from Kielland (1937) for other charged ions; m_i is the molal concentration and z_i the charge of the ith aqueous species. The γ_i of neutral species was set to unity, and the γ_i of water was calculated from the osmotic coefficient (Helgeson et al., 1981).

2.4. Derivation of solubility products (K_{s0})

The equilibrium constants for the dissolution of REE phosphates in aqueous solutions as a function of pH are described by the following sets of reactions:

$$\mathrm{REEPO_4}(s) = \mathrm{REE}^{3+} + \mathrm{PO_4^{3-}}\ (K_{\mathrm{s0}}) \tag{3}$$

$$\mathrm{REEPO_4}(s) + \mathrm{H}^+ = \mathrm{REE}^{3+} + \mathrm{HPO_4^{2-}}\ (K_{\mathrm{s1}}) \tag{4}$$

$$\mathrm{REEPO_4}(s) + 2\mathrm{H}^+ = \mathrm{REE}^{3+} + \mathrm{H_2PO_4^{-}}\ (K_{\mathrm{s2}}) \tag{5}$$

$$\mathrm{REEPO_4}(s) + 3\mathrm{H}^+ = \mathrm{REE}^{3+} + \mathrm{H_3PO_4^{0}}\ (K_{\mathrm{s3}}) \tag{6}$$

At a pH of 2, the dominant phosphate species in the experiments were $H_3PO_4^0$ and to a lesser extent $H_2PO_4^-$ (Appendix A.1). The solubility product (K_{s0}) can then be determined from calculated ion activities and Reaction (6),

$$K_{s3} = \frac{a_{\mathrm{REE}^{3+}} \cdot a_{\mathrm{H_3PO_4^0}}}{(a_{\mathrm{H}^+})^3} \tag{7}$$

combined with the deprotonation constants of phosphoric acid,

$$\mathrm{H_3PO_4^0} = \mathrm{H^+} + \mathrm{H_2PO_4^-}\ (K_1) \tag{8}$$

$$\mathrm{H_2PO_4^-} = \mathrm{H^+} + \mathrm{HPO_4^{2-}}\ (K_2) \tag{9}$$

$$\mathrm{HPO_4^{2-}} = \mathrm{H^+} + \mathrm{PO_4^{3-}}\ (K_3) \tag{10}$$

where K_1, K_2, and K_3 are the first, second, and third deprotonation constants of phosphoric acid. The equilibrium constant of Reaction 3 can then be calculated by combining the deprotonation constants of phosphoric acid with Equation 7,

$$K_{s0} = K_{s3} \cdot K_1 \cdot K_2 \cdot K_3 \tag{11}$$

which relates to the calculated activities of REE^{3+} and PO_4^{3-} in Table A.1 according to,

$$K_{s0} = a_{\mathrm{REE}^{3+}} \cdot a_{\mathrm{PO_4^{3-}}} \tag{12}$$

3. Experimental results

3.1. Kinetic experiments

A series of kinetic experiments were carried out for a duration of 4 to 14 days to determine approach to equilibrium between the reacted REE phosphate crystals and the aqueous solutions according to Reaction 10. The activities a_i of REE^{3+} and $H_3PO_4^0$ were calculated from the measured P and REE concentrations (Table A.1). The reaction quotient (Q_{s3}) could then be retrieved for the dissolution reaction of xenotime at the experimental conditions,

$$Q_{s3} = \frac{a_{REE^{3+}} \cdot a_{H_3PO_4^0}}{(a_{H^+})^3} \tag{13}$$

Results from the kinetic experiments are shown in Figure 1 for $HoPO_4$ at 100 °C. The experiments were observed to approach, within experimental uncertainty[1], nearly constant Q_{s3} values ranging between -7.0 and -6.5 after about 7 days of reaction. These results indicate that the synthetic REE phosphate crystals approached equilibrium with the aqueous solutions upon dissolution and with increased reaction time. This is further reflected by the reproducibility of Q_{s0} values determined for duplicate experiments after 14 days of reaction (Table A.1). Similar conclusions were drawn in the xenotime solubility study by Gysi et al. (2015), where steady-state REE concentrations were reached after 10 days of reaction at 100 °C and after only 5 days at 150 °C.

3.2. Solubility products (K_{s0})

---

[1] The uncertainty is defined here as the standard deviation (1σ) of the mean $\log Q_{s3}$ value determined between 7 and 14 days of reaction. The 1σ values are found to be in line with uncertainties observed in previous REE phosphate endmember solubility studies (Gysi et al., 2015, 2018).

Based on the kinetic experiments, the solubility products (K_{s0}) were evaluated in the present study for experiments carried out between 14 to 16 days to ensure approach to equilibrium. The retrieved mean K_{s0} values and their associated uncertainties are listed in Table 2 for experiments carried out between 100 and 250 °C. Figure 2 shows that the REE phosphate solubility is retrograde with temperature, decreasing by several orders-of-magnitude from 100 to 250 °C. Further, the relationship between $\log K_{\mathrm{s0}}$ values and $1/T$ does not vary linearly, which indicates that the enthalpy of reaction for each of the REE phosphate endmembers varies with temperature. Replicate $\log K_{\mathrm{s0}}$ values (2 to 5 repeated experiments) yield mean calculated 1σ values of: 0.22 ± 0.09 (95 % confidence) for $TbPO_4$; 0.10 ± 0.06 for $HoPO_4$; 0.17 ± 0.02 for $TmPO_4$; 0.25 ± 0.06 for $LuPO_4$. These values indicate that the experiments are generally reproducible to within 0.25 $\log K_{\mathrm{s0}}$ units.

3.3. Experimental fits and extrapolations to reference temperature (T_r = 298.15 K) and pressure (P_r = 1 bar)

The empirical solubility data can be fit to the following equation:

$$\log K_{\mathrm{s0}} = A + B \times T + \frac{C}{T} + D \log T \qquad (14)$$

where T is the temperature in Kelvin, and $A - D$ are the fitted coefficients. Four isotherms allow fitting the experimental data to three coefficients, which yield regression coefficients (R^2) between 0.962 and 0.993 for the different REE phosphate endmembers (Table 3, Fit1).

A three coefficients fit allows further deriving enthalpy and entropy values at reference conditions.[2] We employed the method of Gysi et al. (2015,

---

[2] In principle, it is possible to derive a heat capacity function (ΔC_P^0) but fitting four

2018) to extrapolate the empirical fits to a reference temperature of 298.15 K and a pressure of 1 bar (Fig. 3). This method uses available calorimetric data from the REE phosphates to constrain either of the fitted coefficients A or C in Equation 14. Coefficient A can be related to the standard entropy of reaction ($\Delta_r S^0_{T_r}$) and coefficient C to the standard enthalpy of reaction ($\Delta_r \mathrm{H}^0_{T_r,P_r}$) for the dissolution of the REE phosphate endmembers. Appendix B shows the thermodynamic relations between the standard enthalpy and entropy of reaction and the fitted coefficients from the solubility experiments. In turn, if the standard thermodynamic properties of the aqueous species are fixed, then the absolute standard entropy ($S^0_{T_r}$) or the standard enthalpy of formation from the elements ($\Delta_f \mathrm{H}^0_{T_r}$) can be retrieved for the REE phosphates from the regressed coefficients of the solubility data. Table 4 lists available standard thermodynamic properties of $\mathrm{TbPO_4}$, $\mathrm{HoPO_4}$, $\mathrm{TmPO_4}$, and $\mathrm{LuPO_4}$. The standard enthalpy of formation was measured for all four REE phosphate endmembers using oxide-melt solution calorimetry (Ushakov et al., 2001); the standard absolute entropy was determined for $\mathrm{LuPO_4}$ by adiabatic calorimetry (Gavrichev et al., 2006) and from *ab initio* calculations for the other endmembers (Ji et al., 2017).

Results from the regressions of the experimental solubility data are listed in Table 3. The constrained fits where $\Delta_f H^0_{T_r,P_r}$ of the REE phosphate endmembers was fixed and $S^0_{T_r}$ calculated (Table 3, Fit 2), yield entropy values ranging between 108.6 and 151.1 J mol^{-1}K^{-1}. These entropy values are within those listed in Navrotsky et al. (2015) of 117.2 and 142.3 ±12.6

---

experimental isotherms allows deriving only two parameters (a_0 and a_1), which reduces the heat capacity function to $\Delta C^0_P = a_0 + a_1 T$ (Appendix B).

J $\mathrm{mol}^{-1}\mathrm{K}^{-1}$ but are mostly higher than predicted by *ab initio* calculations from Ji et al. (2017). The calculated entropy value of 151.1 J mol^{-1} K^{-1} for $\mathrm{LuPO_4}$ is also higher in comparison to the calorimetric study by Gavrichev et al. (2006) whom reported an entropy value of 99.7 J mol^{-1} K^{-1}.

The constrained fits where $S^0_{T_r}$ of the REE phosphate endmembers was fixed and $\Delta_f H^0_{T_r,P_r}$ calculated (Table 3, Fit 3), yield standard enthalpy of formation values ranging between -1963.7 and -1975.5 kJ mol^{-1}. The calculated enthalpies of $\mathrm{TbPO_4}$ and $\mathrm{HoPO_4}$ differ by 3.9 to 4.9 kJ mol^{-1} in comparison to those reported in the calorimetric study by Ushakov et al. (2001) and their experimental uncertainties. In contrast, the calculated enthalpy values of $\mathrm{TmPO_4}$ and $\mathrm{LuPO_4}$ differ by 7.0 to 17.3 kJ mol^{-1} in comparison to the values reported by Ushakov et al. (2001).

4. Discussion

4.1. Comparison to previous REE phosphate solubility studies

The xenotime solubility constants measured in our study are the first available experimental solubility data for the $\mathrm{TbPO_4}$, $\mathrm{HoPO_4}$, $\mathrm{TmPO_4}$ and $\mathrm{LuPO_4}$ endmembers between 100 and 250 °C. The only other available data available were measured at <100 °C for the hydrated REE phosphates, which include rhabdophane ($\mathrm{REEPO_4 \cdot 0.667H_2O}$; REE = La − Dy) and churchite ($\mathrm{REEPO_4 \cdot 2H_2O}$; REE = Gd − Lu and Y). These phases are monoclinic and contain water in their crystal structures (Mesbah et al., 2017; Ochiai and Utsunomiya, 2017; Subramani et al., 2019). Several studies have also shown that the hydrated REE phosphates are metastable phases that control solubility at <100 °C (Gausse et al., 2016; Arinicheva et al., 2018; Shelyug et al., 2018; Subramani et al., 2019). Comparison of the fitted solubility data of xenotime with the hydrated REE phosphates indicates that the latter generally have higher measured solubilities (Fig. 3). Similar observations were made in our previous solubility experiments, with both, xenotime-type (Gysi et al., 2015) and monazite-type endmembers (Gysi et al., 2018).

Another comparison can be made by calculating the logK_{s0} values resulting from a combination of thermodynamic properties of REE phosphates (Table 4) and the thermodynamic properties of aqueous PO_4^{3-} and REE^{3+} species from Supcrt92 (Shock and Helgeson, 1988; Shock et al., 1997). Figure 3 shows that the predicted solubilities generally show significant discrepancies in comparison to our experimental solubility data, especially for the $TbPO_4$ and $LuPO_4$ endmembers. Previous solubility studies for the other monazite and xenotime endmembers (Gysi et al., 2015, 2018) indicate that these discrepancies result from an incompatibility between the measured calorimetric data of the minerals combined with the thermodynamic properties of aqueous species from the Supcrt92 dataset.

4.2. Reconciling calorimetric data of REE phosphates and thermodynamic properties of aqueous REE species with the solubility data

Two different optimization techniques are further evaluated here: i) one focusing on the optimization of thermodynamic data for the REE phosphates similar to the approach by Gysi et al. (2015) for the xenotime solubility; ii) the other one focusing on the optimization of the enthalpy of the aqueous REE species similar to the approach by Gysi et al. (2018) for the monazite solubility.

4.2.1. Solubility predictions using the optimized enthalpy of the REE phosphates and available data for aqueous REE species

Adjusting the standard enthalpy of formation for the REE phosphates (Table 3; Fit3) does not allow reconciling the thermodynamic data available in the literature with the measured solubility data. Figure 3 shows the predicted $\log K_{s0}$ values as a function of temperature using the adjusted REE phosphate enthalpies combined with the aqueous species from Supcrt92 (Supcrt92+ΔH_f^0 mineral optimized). The poor agreement between the predicted $\log K_{s0}$ and the experimental solubility data indicates a need to revise the thermodynamic data for the aqueous REE species. A similar observation was made by Gysi et al. (2018) for the solubility products of $CePO_4$, $SmPO_4$, and $GdPO_4$. In contrast, optimizations of enthalpies for YPO_4, $DyPO_4$, $ErPO_4$, and YPO_4 allowed reconciling the thermodynamic data with the solubility data in the study by Gysi et al. (2015). For accurate solubility calculations, we therefore recommend to use the $\log K_{s0}$ coefficients derived from Fit3 (Table 3) in combination with Equation 14 between 25 – 250 °C for $TbPO_4$, $HoPO_4$, $TmPO_4$, and $LuPO_4$ rather than the optimized mineral enthalpy values.

4.2.2. Thermodynamic optimization of REE^{3+} and REEOH^{2+} for improved modeling

The thermodynamic data and HKF parameters for the REE hydroxyl species were taken in the present study from the estimates of Haas et al. (1995). The two major REE aqueous species considered to be stable at the experimental conditions are REE^{3+} and $REEOH^{2+}$ (Appendix A.1), and therefore, revision of the thermodynamic properties of these two species may be necessary.

At the present time, the only high temperature potentiometric measurements of the first REE hydrolysis constants were undertaken for $NdOH^{2+}$ at 250 and 290 °C by Wood et al. (2002), which seem to be more negative than those predicted by Haas et al. (1995). In contrast, the study of Pourtier et al. (2010) determined the solubility of $NdPO_4$ from 300 to 800 °C and 2 kbar, and concluded that at 300 °C the $Nd(OH)^{2+}$ species needs to have a stronger contribution over the Nd^{3+} species in the low pH range. These observations agree better with the predictions of Haas et al. (1995). According to Migdisov et al. (2016), the calculated activities of REE aqueous species using the data from Haas et al. (1995) may result in a significant overestimation of the stability of REE hydroxyl over the REE^{3+} complexes. Nonetheless, findings from hydrothermal REE phosphate solubility experiments indicate that REE hydroxyl complexes may contribute to measured REE phosphate solubilities at low pH and with increased temperature (Pourtier et al. (2010); Gysi et al. (2018); see also Table A.1). The impact of these observed differences on the calculated activities of Tb^{3+}, Ho^{3+}, Tm^{3+}, and Lu^{3+} are difficult to evaluate because the thermodynamic properties of REE hydroxyl species have not yet been determined experimentally above 100 °C.

To address this issue, a thermodynamic optimization approach can be used to fit the experimental solubility data and retrieve provisional thermodynamic properties for the REE aqueous species. The global optimization algorithm GEMSFITS (Miron et al., 2015) was used in the present study to evaluate whether the solubility data can be reconciled with the standard Gibbs energies of reaction resulting from a combination of the thermodynamic data for aqueous species and the calorimetric data of the REE phosphates. This program is combined with the GEMS3K numerical kernel for Gibbs energy minimization (Kulik et al., 2013), and permits adjusting the standard Gibbs energy of formation of selected REE aqueous species at 298.15 K and 1 bar while recalculating their activities and speciation in the experiments. The optimization task is similar to that used in the monazite solubility study by Gysi et al. (2018), and aims at minimizing the residuals between the calculated dissolved REE and P concentrations in solution and the measured values of the experiments assuming equilibrium with the respective xenotime endmember compositions. This optimization technique permits retrieving revised values for the standard Gibbs energy of formation ($\Delta_f G^0_{Tr,Pr}$) of the aqueous REE species predominant at the experimental conditions. Both REE^{3+} and $REEOH^{2+}$, can be evaluated using this optimization method due to the increased dominance of the REE hydroxyl species with temperature (Table A.1).

Discrepancies observed between the calorimetric data from the REE phosphates (Table 4) and the aqueous REE species from the Supcrt92 dataset (Table 1) can be resolved by either adjusting the standard molal Gibbs energy of REE^{3+} and $REEOH^{2+}$ (Mode I) or by adjusting the standard Gibbs energy of $REEPO_4$(s) and $REEOH^{2+}$ (Mode II) during the optimization.[3] The $\Delta_f G^0_{Tr,Pr}$ values generated using this method should be viewed as provisional and a matter of convenience for thermodynamic modeling because revising the HKF correlation parameters would require new high tempera-

---

[3] The covariance of fitted parameters can be determined in GEMSFITS through repeated Monte Carlo simulations (Miron et al., 2015).

ture empirical data for the aqueous REE species. In addition, this method allows maintaining internal consistency with the association constants reported in Haas et al. (1995) for other REE hydroxyl complexes that cannot be evaluated at the experimental conditions (Table 5 footnote).

The optimized standard Gibbs energies for the different aqueous species and REE phosphates are listed in Table 5. Figure 4 compares the solubility calculations using the optimized aqueous species versus using the REE species from the Supcrt92 dataset. Adjusting the standard Gibbs energy of formation of both, REE^{3+} and REEOH^{2+} (Mode I), yields in most cases the lowest residuals between the experimental and calculated REE solubilities. The parameter optimizations further show that the Tb, Ho, and Tm aqueous species need the largest standard Gibbs energy adjustments, whereas Lu requires the least adjustment. From these optimized thermodynamic properties, the solubility products were re-evaluated with updated $\log K_{\mathrm{s0}}$ values listed in Table 6. Figure 5 compares the optimized $\log K_{\mathrm{s0}}$ values of the different xenotime endmembers. These new values show a systematic decrease in the solubility of the REE phosphates in the order Tb > Ho > Tm > Lu.

The available standard thermodynamic properties of REE aqueous species (Table 1) can be combined with the provisional revised $\Delta_f G^0_{Tr,Pr}$ values listed in Table 5 for improved thermodynamic modeling of the REE phosphate solubilities. However, it is recommended to use adjustments from optimization Mode II if internal consistency needs to be maintained with previously measured properties of aqueous REE chlorides, fluorides and other complexes (Migdisov et al., 2009, 2016) because most of these experimental data rely on the properties of REE^{3+} from the Supcrt92 dataset. Further evaluation of the accuracy of these optimized values can be made once high temperature experimental data become available for REE hydroxyl species.

5. Implications for predicting the solubility of xenotime in hydrothermal fluids

5.1. Numerical modeling of xenotime-fluid REE partitioning

Here we demonstrate an application of the optimized thermodynamic data from the solubility experiments for simulating the partitioning of REE between an ideal xenotime solid solution and an acidic hydrothermal fluid (pH of 2) reacted with 1 g leucogranite per kg H_2O. This model permits simulating the REE composition of xenotime in a hydrothermal quartz-topaz vein with a NaCl-HCl-H_2O fluid saturated with fluorapatite from 100 to 300 °C. The initial REE concentrations of the aqueous fluid was set to chondritic values (McDonough and Sun, 1995) to approximate relative abundances observed in crustal rocks: Y (1.57 ppm) $>$ Dy (246 ppb), Er (160 ppb), Yb (161 ppb) $>$ Ho (54.6 ppb), Tb (36.1 ppb), Tm (24.7 ppb), Lu (24.6 ppb).

Geochemical modeling was carried out using the GEMS code package (Kulik et al., 2013) and the MINES thermodynamic database (Gysi, 2017). Thermodynamic data of aqueous REE chloride complexes were taken from the experiments of Migdisov et al. (2009) and *ab initio* calculations of Guan et al. (2020) for Y chloride species; REE^{3+} and REE hydroxyl complexes were taken from the Supcrt92 database (Haas et al., 1995) and using the optimized values from the solubility experiments (Table 5).

Two ideal xenotime solid solutions were set up comprising all the heavy REE xenotime endmembers (i.e., $TbPO_4$ to $LuPO_4$) to evaluate the impact of the optimized thermodynamic data for xenotime retrieved from the solubility experiments. The first xenotime solid solution utilized the newly optimized dataset from the present study (Table 5) combined with the data for YPO_4, $ErPO_4$, $DyPO_4$ and $YbPO_4$ from Gysi et al. (2015). The second solid solution utilized the previously available calorimetric data of xenotime (Table 4).

The simulation results are depicted in Figure 6 for predicted REE partition coefficients ($D_{\text{REE, xnt-fluid}}$) and mole fraction REE in xenotime at temperatures between 100 and 300 °C at saturated water vapor pressure. The partition coefficients were calculated according to:

$$D_{\text{REE, xnt-fluid}} = \frac{X_{\text{REE, xnt}}}{(m_{\text{REE}}/m_{\text{tot,REE}})} \tag{15}$$

where $X_{\text{REE,xnt}}$ represents the calculated mole fraction REE in xenotime; m_{REE} is the molality (mol/kg) REE in the aqueous fluid; $m_{\text{tot,REE}}$ is the total dissolved REE molality in the aqueous fluid.

The REE partition coefficients calculated from the optimized thermodynamic data differ significantly from those predicted using the Supcrt92 dataset combined with the calorimetric data of the REE phosphates (Fig. 6). The optimized simulations indicate that the heavy REE with higher atomic numbers and lower ionic radii (Tm, Yb, and Lu) are less soluble than the other REE (Er, Dy, Ho, and Tb) and therefore more likely to be enriched in the xenotime solid solution relative to the aqueous fluid (Fig. 6a). An opposite trend is observed in the non-optimized simulations (Fig. 6b) as illustrated by the behavior of Lu and Yb that are more soluble in the aqueous fluid in comparison to most other heavy REE up to 300 °C (Fig. 6b). This trend is inconsistent with the measured REE phosphate solubility data

(Fig. 5), and therefore using the optimized thermodynamic data derived in this study improves the model considerably. In contrast to the calculated partition coefficients, the simulated mole fractions of REE in xenotime are similar in both models (Figs. 6b,d) because the input REE concentrations of the model significantly controls the simulated mineral composition at supersaturation.

Although these simulations depict a simplified scenario, it has to be considered that the variations observed in natural solid solutions and REE aqueous species are controlled by several competing mechanisms. These include the solubility of the REE phosphates as a function of temperature, the relative abundance of available REE in the source rock or fluid, and the stability of different REE aqueous species as a function of temperature and pH. Figure 7 shows the aqueous species expected to control the solubility of REE in the aqueous fluid between 100 and 300 °C and pH of 2. The REE^{3+} ion is predominant for most heavy REE, particularly Lu^{3+}, Tm^{3+}, and Y^{3+}, whereas REE chloride species (i.e., $REECl^{2+}$) predominate above 250 °C for heavy REE with larger ionic radii, including Tb and Ho. These simulations indicate that using the provisional optimized thermodynamic data from Table 5 will not affect aqueous speciation in an acidic saline fluid because the REE hydroxyl complexes are not predominant at these conditions. Nevertheless, the REE hydroxyl species are expected to become significant in more alkaline aqueous fluids, such as those predicted to be in equilibrium with a calcite vein (Perry and Gysi (2018)).

For comparison, we also show the simulated Y chloride species using the recent data of Guan et al. (2020) derived from *ab initio* molecular dynamic simulations (Fig. 7c). The predicted aqueous Y chloride species that predominate between 250 and 300 °C include YCl_2^+, YCl_3^0, and YCl_4^-. It is possible that the Y chloride species derived from molecular dynamic simulations overestimate the coordination of Y-Cl at lower temperatures (Guan et al., 2020). This could potentially explain why the $REECl^{2+}$ species is not predominant over other Y chloride species in comparison to the other REE in the simulated temperature range. Consideration of the Y chloride species in test simulations led to an overestimation in the Y solubility and a drastic shift in all calculated REE partition coefficients above 250 °C.

5.2. Compositions of hydrothermal xenotime in natural systems

In natural systems, xenotime has been observed to be associated with hydrothermal alteration textures, and in some cases, records relatively low formation temperatures. Hydrothermal xenotime has been reported from hydrothermal alteration zones in carbonatite and alkaline complexes which host potential REE deposits such as Bear Lodge in Wyoming (Andersen et al., 2016, 2017, 2019) and Lofdal in Namibia (Wall et al., 2008; Bodeving et al., 2017). In the Pea Ridge iron-oxide-apatite (IOA) − REE deposit, Missouri, for example, metasomatic replacement of apatite and associated reactions led to the formation of xenotime at temperatures between 100 and 400 °C (Harlov et al., 2016; Hofstra et al., 2016; Mercer et al., 2020). Both xenotime and monazite, have also been reported to record hydrothermal evolution during tectonic events in metasomatised Precambrian metasedimentary rocks and ore deposits of Australia at temperatures generally < 400 °C (Rasmussen et al., 2007, 2011; Zi et al., 2015; McNaughton and Rasmussen, 2018). Fluid inclusions from the sediment-hosted xenotime REE deposit in the Browns Range (Australia) further record temperatures as low as 100 − 120 °C (Richter et al., 2018).

Figure 8 shows a compilation of the range of REE abundances observed in natural xenotime associated with the REE mineral deposits described above. The chondrite normalized REE profiles indicate significant variations in the heavier REE including Er, Tm, Yb, and Lu. Comparison of these variations to the numerical simulations indicates that temperature and the relative solubility of the different REE phosphate endemembers play a significant role in partitioning of REE during the formation of xenotime from a hydrothermal fluid. Xenotime exhibits lower Er, Tm, Yb, and Lu values in the simulations performed at 300 °C than at 100 °C. Although the simulations do not aim to simulate the exact formation conditions of the natural REE deposits, it is interesting to note that the xenotime from IOA deposit in Pea Ridge is generally enriched the heavier REE in comparison to xenotime formed in the carbonatites which are depleted in them. This example shows one application of the optimized thermodynamic data for simulating the composition of xenotime but additional parameters can be tested including fluid chemistry, source of REE abundance, salinity, and pH. It is also interesting to note that the chondrite normalized REE profiles of the simulated xenotime compositions are within the range of those observed from the natural data. This indicates that the precipitation of xenotime in the model led to an enrichment of the initial chondritic REE values of the fluid by several orders of magnitude.

Future models may consider that xenotime most likely forms a non-ideal solid solution, especially for the incorporation of REE whose ionic radii are significantly different from Y^{3+}. To our knowledge, solid solution properties have not yet been determined experimentally for YPO_4 and other REE phosphates with the xenotime structure. In binary monazite solid solutions, excess enthalpy of mixing has been determined by high temperature solution calorimetry, which suggests non-ideal mixing behavior in the monazite structure (Popa et al., 2007; Neumeier et al., 2017). Structural and spectroscopic measurements have further detected significant excess molar volumes in La-Eu and La-Gd monazite solid solutions (Geisler et al., 2016), whereas for La-Pr monazite solid solutions no significant excess properties were detected (Hirsch et al., 2017). These observations are supported by *ab initio* calculations and indicate that the volume mismatch between REE with different ionic sizes results in increased non-ideal mixing behavior (Li et al., 2014). A similar behavior is likely to be expected for binary xenotime solid solutions and this needs to be accounted for in more realistic numerical models.

6. Conclusions

We have measured the solubility of synthetic $TbPO_4$, $HoPO_4$, $TmPO_4$, and $LuPO_4$ endmembers in aqueous solutions at temperatures from 100 to 250 °C at saturated water vapor pressure. The REE phosphates with the xenotime structure display a retrograde solubility and extrapolation to reference temperature and pressure yields lower solubilities than measured for the hydrated REE phosphates (i.e., rhabdophane and churchite).

Combining calorimetric data of the REE phosphates with the thermodynamic properties of aqueous species from the Supcrt92 dataset (Shock and Helgeson, 1988; Haas et al., 1995; Shock et al., 1997) yields solubilities lower than those observed in the experiments (Fig. 4). Using data from the solubility experiments, the compatibility of these different datasets can be optimized by: (i) adjusting the standard enthalpy of formation of the solid endmembers (Gysi et al., 2015), or (ii) adjusting the standard Gibbs energy of the aqueous REE species (Gysi et al., 2018). Here we recommend a set of provisional revised standard Gibbs energies of aqueous REE species and enthalpies for REE phosphates listed in Table 5 and the updated solubility products listed in Table 6. These optimizations indicate the need of future experimental measurements to accurately determine the speciation of REE hydroxyl complexes as a function of pH and temperature especially in alkaline systems where these complexes may become dominant. Together with the data presented in the study of Gysi et al. (2015), our work completes the xenotime endmember solubility series between 100 and 250 °C and provides a solid framework for future improvement in our understanding of REE solubility in natural hydrothermal systems.

Acknowledgments

This project was supported by the National Science Foundation to APG (NSF grant EAR-2032761). We would like to thank K. Challis and J. Ranville from the Colorado School of Mines for assistance on the ICP-MS instrument, and N. Iverson from the New Mexico Institute of Mining and Technology for help with scanning electron microscope imaging. We are grateful for the constructive comments by Marion Louvel and two anonymous reviewers, and would like to thank Editor M.E. Böttcher for handling this manuscript.

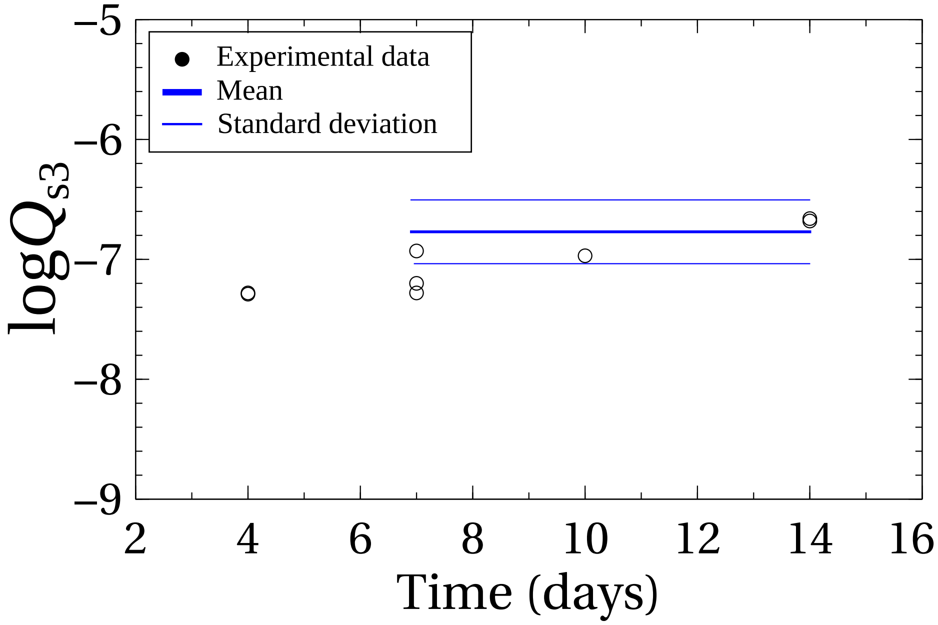

Figure 1: Kinetic experiments at 100 °C and saturated water vapor pressure showing the logarithm of the reaction quotient (Q_{s3}) for the solubility of $HoPO_4$ as a function of reaction time. The lines show the mean and standard deviation of the experimental data suggesting approach to a steady-state after 7 days of reaction.

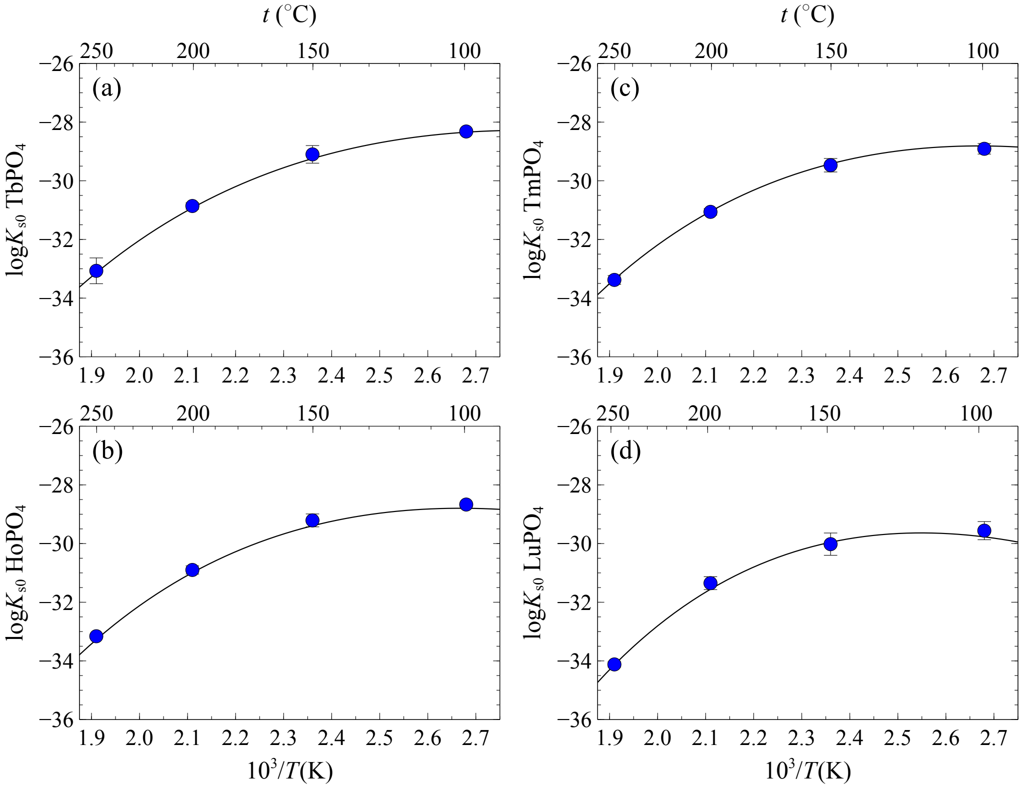

Figure 2: Logarithm of solubility products (K_{s0}) of REE phosphates vs. the inverse of temperature ($1/T$ in K^{-1}) calculated from the experimental data collected between 100 and 250 °C and saturated water vapor pressure. The experimental data (symbols) and regressions from Fit1 (curves) are reported in Tables 2 and 3. The error bars or symbol sizes represent the 1σ from 2 to 5 repeated experiments.

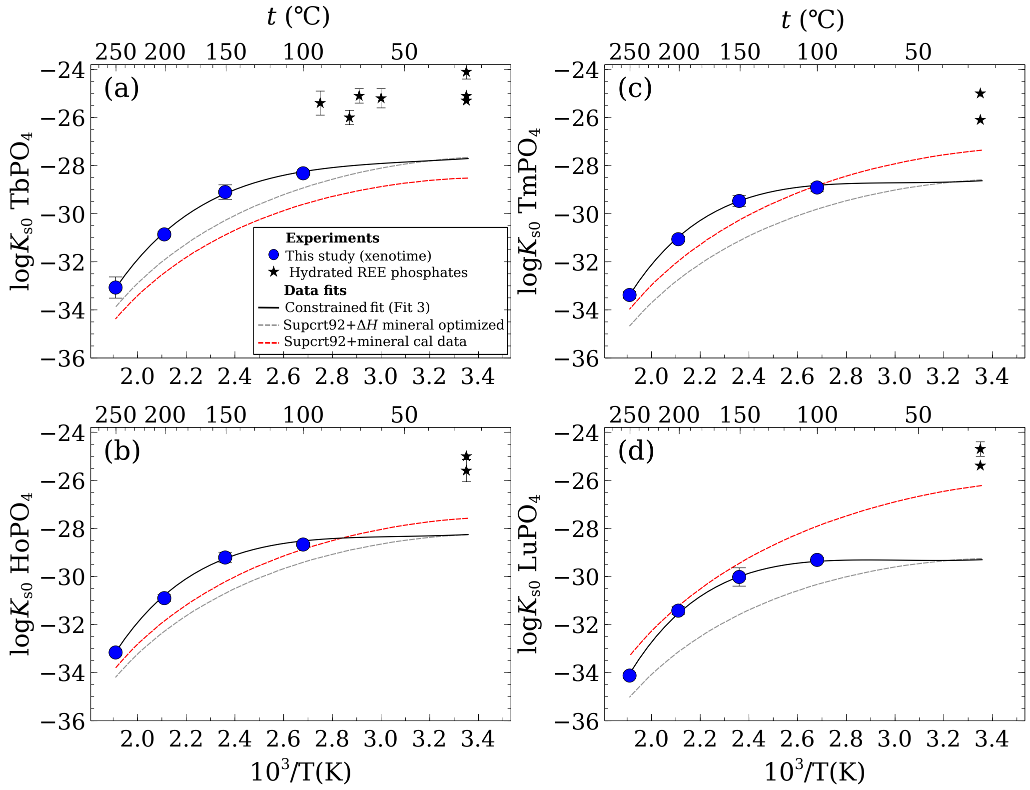

Figure 3: Logarithm of solubility products (K_{s0}) of xenotime endmembers vs. the inverse of temperature ($1/T$ in K) calculated from the experimental data collected between 100 and 250 °C. The xenotime solubility data and regressions from Fit3 are reported in Tables 2 and 3. Supcrt92+mineral cal data: calculated K_{s0} values retrieved by combining the calorimetric data of REE phosphates listed in Table 4 and the thermodynamic properties of aqueous species for REE^{3+} and PO_4^{3-} from the Supcrt92 database (Shock and Helgeson, 1988; Shock et al., 1997). Supcrt92+$\Delta_f H^0$ mineral optimized: recalculated K_{s0} values using the standard enthalpies derived from Fit 3 in Table 3 for each REE phosphate. For comparison, solubility data for the metastable and hydrated REE phosphates are shown < 100 °C (Firsching and Brune, 1991; Liu and Byrne, 1997; Gausse et al., 2016). The error bars (or symbol sizes) represent the standard deviation (1σ) from 2 to 5 repeated experiments.

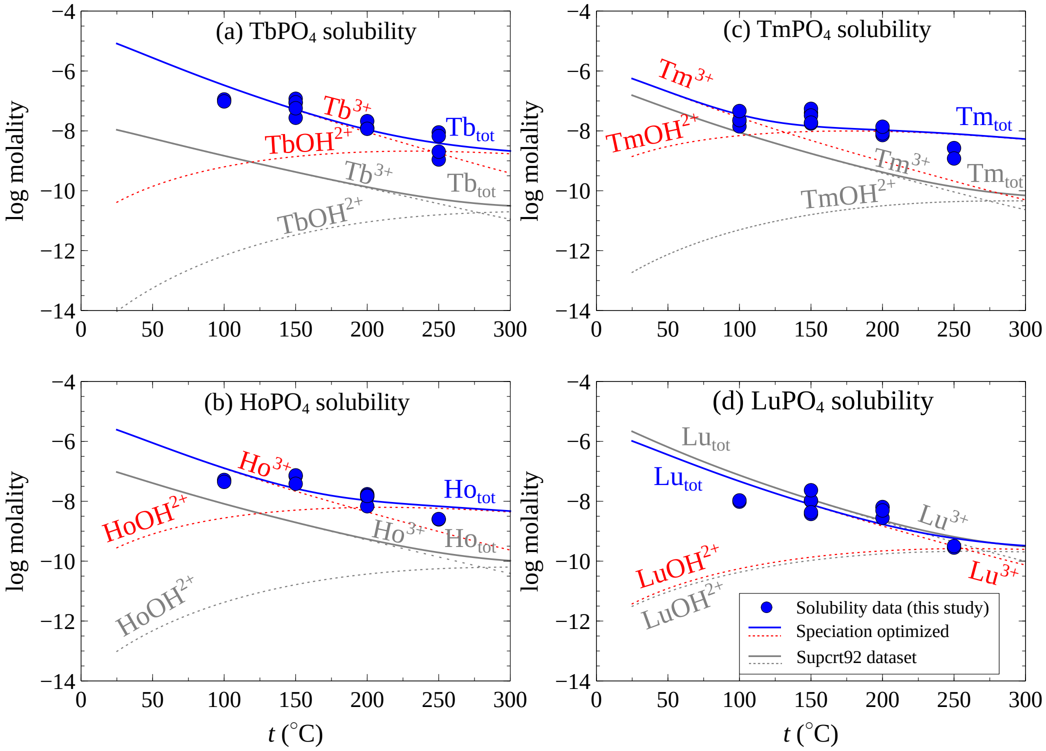

Figure 4: Comparison between experimental data and calculated solubilities of (a) $TbPO_4$, (b) $HoPO_4$, (c) $TmPO_4$, and (d) $LuPO_4$ as a function of temperature showing the total dissolved REE molalities (solid lines) and predominant REE aqueous species (dashed lines). The optimized standard Gibbs energy of formation values for aqueous REE species were taken from Table 5 and are compared to calculations using the standard thermodynamic properties from the Supcrt92 dataset (Shock and Helgeson, 1988; Haas et al., 1995; Shock et al., 1997).

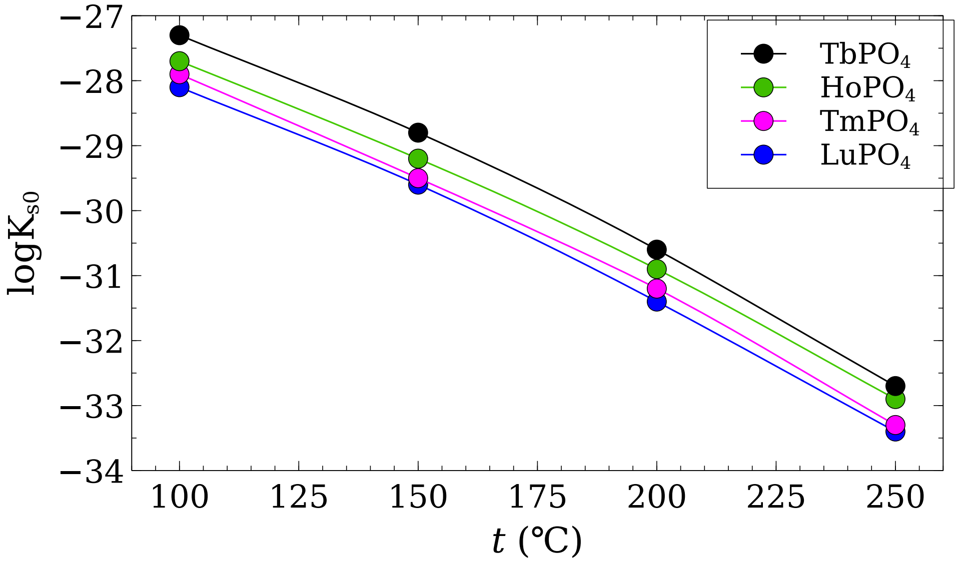

Figure 5: Comparison of the optimized solubility products ($\log K_{s0}$) of $TbPO_4$ (Mode I-II), $HoPO_4$ (Mode I-II), $TmPO_4$ (Mode II), and $LuPO_4$ (Mode I-II) as a function of temperature. Thermodynamic data for optimized aqueous REE species were taken from Table 5 and used to re-evaluate calculated REE^{3+} activities listed in Table A.1.

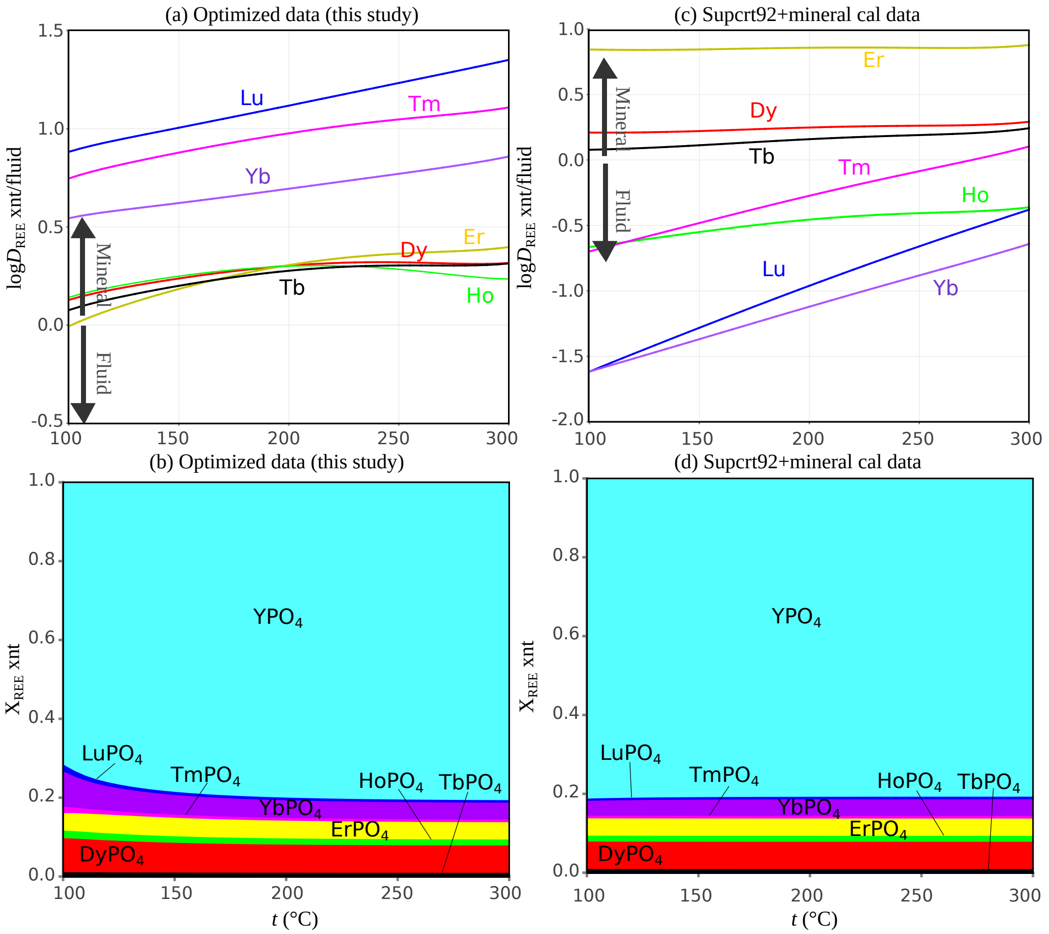

Figure 6: Simulated REE partition coefficients (D_{REE}) and mole fraction REE in xenotime (X_{REE}) for an ideal xenotime solid solution in equilibrium with 1000 g of an acidic saline hydrothermal fluid cooled from 300 to 100 °C at saturated water vapor pressure. The initial fluid (pH of 2, 0.05 m HCl, 10 wt.% NaCl, 50 ppm P) had REE concentrations using chondritic abundances (McDonough and Sun, 1995) and was reacted with 1 g of leucogranite (35 wt.% quartz, 29 wt.% albite, 17 wt.% microcline, and 19 wt.% muscovite). (a,b) Simulations using the optimized thermodynamic data from the solubility experiments (Table 5 and Gysi et al. (2015)). (c,d) Simulations using the Supcrt92 dataset for aqueous species (Shock and Helgeson, 1988; Haas et al., 1995; Shock et al., 1997) combined with calorimetric data for minerals (Table 4 and Gysi et al. (2015)).

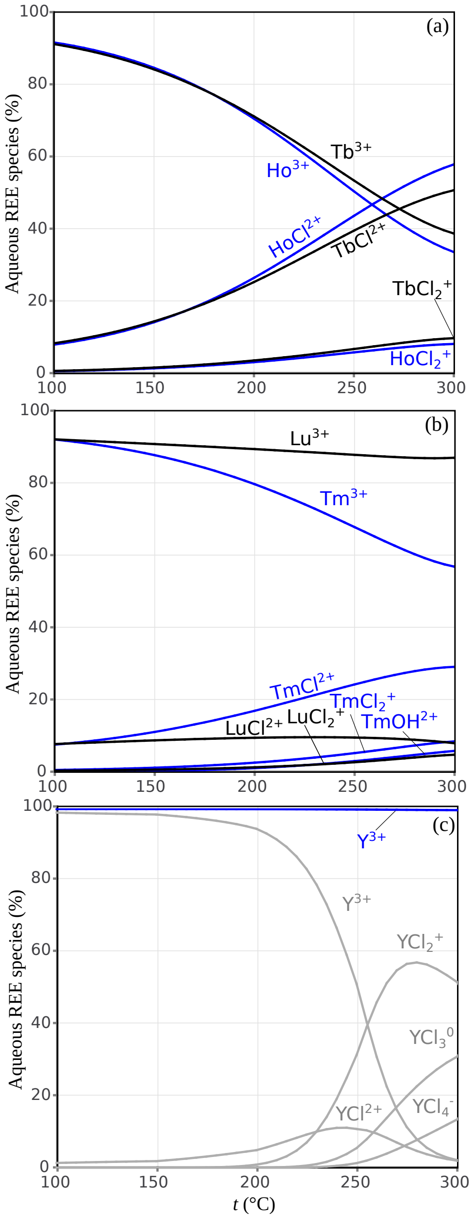

Figure 7: Simulated abundance (in %) of REE aqueous species at a pH of 2 for an ideal xenotime solid solution in equilibrium with 1000 g of an acidic saline hydrothermal fluid cooled from 300 to 100 °C at saturated water vapor pressure. The model corresponds to the simulations using the optimized thermodynamic data from this study (Fig. 6a,b). Gray lines in (c) show simulations that include the Y chloride species derived from Guan et al. (2020).

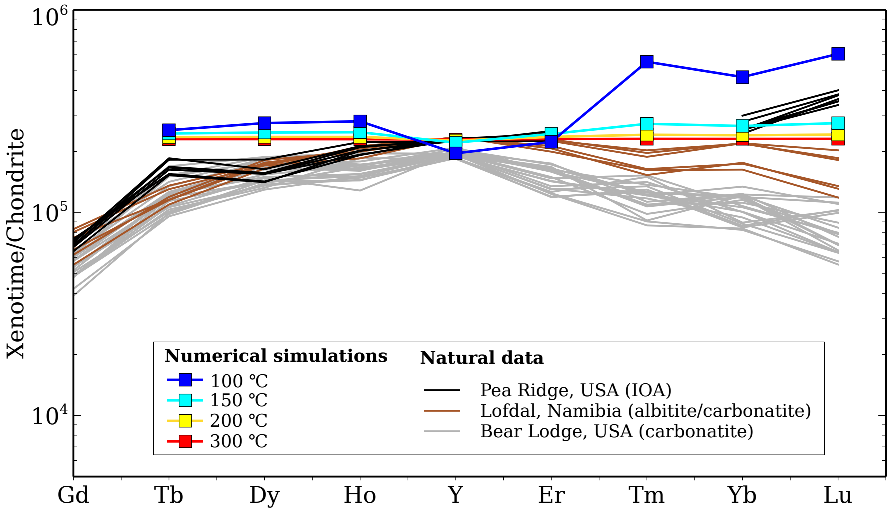

Figure 8: Chondrite normalized (McDonough and Sun, 1995) REE profiles in natural xenotime compared to simulated compositions between 100 and 300 °C at saturated water vapor pressure. Natural data: Pea Ridge iron-oxide-apatite (IOA)−REE deposit, Missouri, USA (Harlov et al., 2016); Lofdal carbonatite/albitite, Namibia (Wall et al., 2008); Bear Lodge carbonatite/alkaline complex, Wyoming, USA (Andersen et al., 2016).

Table 1: Sources of thermodynamic data from the Supcrt92 dataset considered in the aqueous speciation calculations.

Species	Ref.
REE-species (Tb, Ho, Tm, and Lu)	
REE^{3+}	1, 2
$REE(OH)_3^0$, $REE(OH)_2^+$, $REE(OH)^{+2}$, $REE(OH)_4^-$	3
Major P-species	
$H_3PO_4^0$	4
$H_2PO_4^-$, HPO_4^{2-}, PO_4^{3-}	1, 2
Minor P-species	
$H_2P_2O_7^{2-}$, $H_3P_2O_7^-$, $H_4P_2O_7^0$, $HP_2O_7^{3-}$, $P_2O_7^{4-}$	1, 2
Other species	
OH^-, H^+	1, 2
ClO_4^-	1, 2

References:[1] Shock et al. (1997); [2] Shock and Helgeson (1988); [3]Haas et al. (1995); [4]Shock et al. (1989)

Table 2: Values of the logarithm of the solubility product (K_{s0}) of REE phosphates determined experimentally at temperature (t) and saturated water vapor pressure.

t (°C)	logK_{s0} $TbPO_4$	σ	logK_{s0} $HoPO_4$	σ	logK_{s0} $TmPO_4$	σ	logK_{s0} $LuPO_4$	σ
100	-28.32	0.05	-28.67	0.01	-28.91	0.18	-29.31	0.10
150	-29.10	0.30	-29.21	0.22	-29.47	0.23	-30.02	0.38
200	-30.86	0.11	-30.90	0.14	-31.06	0.11	-31.42	0.17
250	-33.07	0.44	-33.16	0.01	-33.38	0.15	-34.12	0.09

The standard deviation of the mean (σ) was calculated based on 2 to 5 repeated experiments (Table A.1).

Table 3: Regressed coefficients ($A - D$, Equation 14) for the temperature dependence (in Kelvin) of the solubility product ($\log K_{s0}$) of REE phosphates determined from the experimental values listed in Table 2. Fit 2 and Fit 3 list the calculated standard enthalpy of formation ($\Delta_f H^0$) and entropy (S^0) values; fixed values were taken from the data listed in Table 4.

	A	B	C	D	R^2	$\log K_{s0,T_r,P_r}$	$\Delta_f H^0_{T_r,P_r}$ kJ mol^{-1}	$S^0_{T_r}$ J mol^{-1} K^{-1}
Fit 1: unconstrained								
$\log K_{s0}$ ($TbPO_4$)	36.80	-0.0913	-1.158×10^4	-	0.965	-	-	-
$\log K_{s0}$ ($HoPO_4$)	50.27	-0.1056	-1.475×10^4	-	0.993	-	-	-
$\log K_{s0}$ ($TmPO_4$)	51.35	-0.1071	-1.503×10^4	-	0.988	-	-	-
$\log K_{s0}$ ($LuPO_4$)	77.03	-0.1361	-2.086×10^4	-	0.962	-	-	-
Fit 2: $\Delta_f H^0$ fixed, S^0 calculated								
$\log K_{s0}$ ($TbPO_4$)	-1138	-3.134×10^{-1}	3.022×10^4	4.456×10^2	0.978	-27.8	-1968.6	108.6
$\log K_{s0}$ ($HoPO_4$)	-1532	-3.955×10^{-1}	4.286×10^4	5.973×10^2	0.990	-28.3	-1971.6	135.2
$\log K_{s0}$ ($TmPO_4$)	-1781	-4.478×10^{-1}	5.087×10^4	6.932×10^2	0.987	-28.6	-1964.7	141.1
$\log K_{s0}$ ($LuPO_4$)	-2007	-4.962×10^{-1}	5.820×10^4	7.803×10^2	0.983	-29.0	-1955.4	151.1
Fit 3: $\Delta_f H^0$ calculated, S^0 fixed								
$\log K_{s0}$ ($TbPO_4$)	-1212	-3.271×10^{-1}	3.287×10^4	4.736×10^2	0.978	-27.7	-1963.7	123.1
$\log K_{s0}$ ($HoPO_4$)	-1483	-3.867×10^{-1}	4.105×10^4	5.789×10^2	0.991	-28.3	-1975.5	123.8
$\log K_{s0}$ ($TmPO_4$)	-1684	-4.299×10^{-1}	4.734×10^4	6.564×10^2	0.988	-28.7	-1971.7	120.5
$\log K_{s0}$ ($LuPO_4$)	-1756	-4.498×10^{-1}	4.914×10^4	6.855×10^2	0.982	-29.3	-1972.7	99.7

Table 4: Standard thermodynamic properties of REE phosphates retrieved from calorimetric and *ab initio* studies at reference temperature (T_r) and pressure (P_r) of 298.15 K and 1 bar. The heat capacity function is described by $C_{P,T}$=a+bT+c/T^2 with coefficients fitted in this study and C_{P,T_r} calculated from the fits.

	$\Delta_f H^0_{T_r,P_r}$ kJ mol^{-1}	$S^0_{T_r}$ J mol^{-1} K^{-1}	V_m cm^3 mol^{-1}	C_{P,T_r} J mol^{-1}K^{-1}	a	b	c
$TbPO_4$	-1968.6[1] ±4.6	123.1[3]	43.9[2]	105.3[7]	116.4	0.0455	-2.19×10^6
$HoPO_4$	-1971.6[1] ±3.4	123.8[3]	42.9[2]	102.1[4]	124.4	0.0266	-2.69×10^6
$TmPO_4$	-1964.7[1] ±4.7	120.5[3]	42.0[2]	99.7[8]	128.8	0.0190	-3.09×10^6
$LuPO_4$	-1955.4[1] ±4.2	99.7[5] ±0.3	41.2[2]	99.7[5,6]	130.7	0.0185	-3.33×10^6

References: [1]Ushakov et al. (2001), oxide-melt solution calorimetry; [2]Ni et al. (1995), x-ray diffraction; [3]Ji et al. (2017), *ab initio* calculations; [4]Tyurin et al. (2020), adiabatic and differential scanning calorimetry; [5]Gavrichev et al. (2006), adiabatic calorimetry; [6]Nikiforova et al. (2012), drop calorimetry; [7]Gavrichev et al. (2013), adiabatic calorimetry; [8]This study, estimated by interpolation of C_P function of $TbPO_4$, $HoPO_4$, and $LuPO_4$, and the ionic radii of REE^{3+} in 8-fold coordination (Shannon, 1976).

Table 5: Provisional revised values of the standard molal Gibbs energy of aqueous REE species from Supcrt92 optimized using GEMSFITS. Optimizations include Mode I (REE^{3+} and $REEOH^{2+}$) and Mode II ($REEOH^{2+}$ and $REEPO_4$(s)).

Species	$\Delta_f G^0_{298.15K,1bar}$ (Supcrt 92) J mol^{-1}	$\Delta_f G^0_{298.15K,1bar}$ (Mode I) J mol^{-1}	σ J mol^{-1}		$\Delta_f G^0_{298.15K,1bar}$ (Mode II) J mol^{-1}	σ J mol^{-1}	
Tb^{3+}	-667,348	-684,086	834	Opt	-	-	Fixed
$TbOH^{2+}$	-859,812	-880,897	6,442	Opt	-864,158	4,551	Opt
TbO^+	-812,114	-833,199	-	C^a	-816,469	-	C^a
TbO_2^-	-946,421	-967,506	-	C^b	-950,767	-	C^b
TbO_2H^0	-998,721	-1,019,806	-	C^c	-1,003,067	-	C^c
$TbPO_4$(s)	-1,848,897	-	-	F	-1,832,162	965	Opt
Ho^{3+}	-675,298	-683,662	1,007	Opt	-	-	F
$HoOH^{2+}$	-868,180	-888,220	1,612	Opt	-871,180	4,368	Opt
HoO^+	-820,901	-840,941	-	C^a	-823,901	-	C^a
HoO_2^-	-958,554	-978,594	-	C^b	-961,554	-	C^b
HoO_2H^0	-1,009,599	-1,029,640	-	C^c	-1,012,599	-	C^c

$HoPO_4(s)$	-1,851,486	-	-	F	-1,840,522	359	Opt
Tm^{3+}	-669,022	-672,494	1,447	Opt	-	-	F
$TmOH^{2+}$	-862,322	-884,708	883	Opt	-872,603	3,039	Opt
TmO^{+}	-815,462	-837,848	-	C^a	-825,743	-	C^a
TmO_2^-	-956,881	-979,267	-	C^b	-967,162	-	C^b
TmO_2H^0	-1,005,415	-1,027,801	-	C^c	-1,015,696	-	C^c
$TmPO_4$	-1,843,986	-	-	F	-1837596	713	Opt
Lu^{3+}	-666,930	-665,402	1,154	Opt	-	-	F
$LuOH^{2+}$	-860,649	-861,414	4,883	Opt	-856,478	1,178	Opt
LuO^{+}	-816,717	-817,482	-	C^a	-812,546	-	C^a
LuO_2^-	-958,973	-959,738	-	C^b	-954802	-	C^b
LuO_2H^0	-1,004,997	-1,005,762	-	C^c	-1,000,826	-	C^c
$LuPO_4(s)$	-1,835,369	-	-	F	-1,836,509	384	Opt

Opt: Optimized; C: Constrained; F: Fixed. The convention used in Supcrt92 allows conversion to the hydrated species: $REEO^+ + H_2O = REE(OH)^{2+}$, $REEO_2^- + 2H_2O = REE(OH)_4^-$, $REEO_2H^0 + H_2O = REE(OH)_3^0$. Association constants were constrained by Haas et al. (1995) according to: $^aREEOH^{2+} = H^+ + REEO^+$; $^bREEOH^{2+} + H_2O = 3H^+ + REEO_2^-$; $^cREEOH^{2+} + H_2O = 2H^+ + REEO_2H^0$. The standard deviation (σ) was calculated from 100 Monte Carlo simulations.

Table 6: Updated values of the REE phosphate solubility products (logK_{s0}) using the optimized thermodynamic data from Table 5 and recalculated from the experimental data. The uncertainties represent the overall reproducibility of the experimental method.

t (°C)	logK_{s0}(TbPO$_4$)	logK_{s0}(HoPO$_4$)	logK_{s0}(TmPO$_4$)	logK_{s0} (LuPO$_4$)
100	-27.3 ±0.25	-27.7 ±0.25	-27.9 ±0.25	-28.1 ±0.25
150	-28.8 ±0.25	-29.2 ±0.25	-29.5 ±0.25	-29.6 ±0.25
200	-30.6 ±0.25	-30.9 ±0.25	-31.2 ±0.25	-31.4 ±0.25
250	-32.7 ±0.25	-32.9 ±0.25	-33.3 ±0.25	-33.4 ±0.25

Appendix A.

Table A.1: Composition of quenched experimental solutions (mol/kg) from solubility experiments performed at temperatures between 100 and 250 °C at saturated water vapor pressure. Also listed are the calculated logarithms from the reaction quotient (Q_{s0}) and activities (a_i) of aqueous species calculated using the thermodynamic data listed in Table 1.

Type	t (°C)	Time (days)	pH$_T$	logQ_{s0}	$m_{\mathrm{ClO_{4^-}}}$	m_{P}	m_{REE}	log$a_{\mathrm{REE^{3+}}}$	log$a_{\mathrm{REEOH^{2+}}}$	log$a_{\mathrm{H_3PO_4}}$	log$a_{\mathrm{H_2PO_4^-}}$	log$a_{\mathrm{HPO_4^{2-}}}$	log$a_{\mathrm{PO_4^{3-}}}$
TbPO$_4$	100	14	2.02	-28.29	1.07×10^{-2}	4.96×10^{-5}	1.12×10^{-7}	-7.42	-10.48	-4.92	-5.49	-10.77	-20.87
	100	14	2.02	-28.35	1.07×10^{-2}	4.99×10^{-5}	9.63×10^{-8}	-7.49	-10.55	-4.92	-5.49	-10.76	-20.86
	150	16	2.01	-28.83	1.09×10^{-2}	7.60×10^{-5}	1.18×10^{-7}	-7.47	-9.27	-4.68	-5.58	-11.09	-21.35
	150	16	2.01	-28.95	1.09×10^{-2}	7.76×10^{-5}	8.65×10^{-8}	-7.61	-9.40	-4.67	-5.57	-11.09	-21.34
	150	16	2.01	-28.94	1.09×10^{-2}	7.67×10^{-5}	8.98×10^{-8}	-7.59	-9.39	-4.67	-5.58	-11.09	-21.35
	150	14	2.01	-29.56	1.09×10^{-2}	5.99×10^{-5}	2.73×10^{-8}	-8.11	-9.90	-4.78	-5.68	-11.20	-21.46
	150	14	2.01	-29.21	1.09×10^{-2}	6.57×10^{-5}	5.71×10^{-8}	-7.79	-9.59	-4.74	-5.64	-11.16	-21.42
	200	14	2.02	-30.86	1.09×10^{-2}	7.70×10^{-5}	1.26×10^{-8}	-8.56	-9.35	-4.64	-5.90	-11.74	-22.30
	200	14	2.03	-30.74	1.07×10^{-2}	5.56×10^{-5}	2.11×10^{-8}	-8.33	-9.11	-4.78	-6.03	-11.86	-22.41
	200	14	2.03	-30.97	1.07×10^{-2}	5.93×10^{-5}	1.17×10^{-8}	-8.59	-9.37	-4.76	-6.00	-11.84	-22.38
	250	14	2.03	-32.66	1.09×10^{-2}	5.67×10^{-5}	8.91×10^{-9}	-8.96	-8.91	-4.76	-6.42	-12.71	-23.70
	250	14	2.03	-32.74	1.09×10^{-2}	6.26×10^{-5}	6.69×10^{-9}	-9.08	-9.04	-4.71	-6.38	-12.67	-23.66
	250	14	2.03	-33.58	1.09×10^{-2}	5.49×10^{-5}	1.10×10^{-9}	-9.86	-9.82	-4.77	-6.44	-12.72	-23.72
	250	14	2.03	-33.29	1.09×10^{-2}	5.89×10^{-5}	2.02×10^{-9}	-9.60	-9.56	-4.74	-6.41	-12.69	-23.69

Type	t (°C)	Time (days)	pH$_T$	logQ_{s0}	$m_{\mathrm{ClO_4^-}}$	m_{P}	m_{REE}	log$a_{\mathrm{REE^{3+}}}$	log$a_{\mathrm{REEOH^{2+}}}$	log$a_{\mathrm{H_3PO_4}}$	log$a_{\mathrm{H_2PO_4^-}}$	log$a_{\mathrm{HPO_4^{2-}}}$	log$a_{\mathrm{PO_4^{3-}}}$
$HoPO_4$	100	4	2.01	-29.29	1.09×10^{-2}	5.02×10^{-5}	1.18×10^{-8}	-8.40	-11.43	-4.91	-5.50	-10.78	-20.89
	100	4	2.01	-29.30	1.09×10^{-2}	5.68×10^{-5}	1.03×10^{-8}	-8.46	-11.49	-4.86	-5.44	-10.72	-20.84
	100	7	2.02	-29.29	1.07×10^{-2}	6.04×10^{-5}	9.26×10^{-9}	-8.51	-11.52	-4.83	-5.41	-10.68	-20.78
	100	7	2.02	-29.21	1.07×10^{-2}	6.21×10^{-5}	1.08×10^{-8}	-8.44	-11.45	-4.82	-5.40	-10.67	-20.77
	100	7	2.02	-28.94	1.07×10^{-2}	5.28×10^{-5}	2.34×10^{-8}	-8.10	-11.12	-4.89	-5.47	-10.74	-20.84
	100	10	2.01	-28.98	1.09×10^{-2}	1.79×10^{-5}	6.91×10^{-8}	-7.64	-10.66	-5.36	-5.95	-11.23	-21.34
	100	14	2.02	-28.66	1.07×10^{-2}	4.55×10^{-5}	5.16×10^{-8}	-7.76	-10.77	-4.96	-5.53	-10.80	-20.90
	100	14	2.02	-28.68	1.07×10^{-2}	5.06×10^{-5}	4.43×10^{-8}	-7.83	-10.84	-4.91	-5.49	-10.76	-20.86
	150	16	2.01	-29.03	1.09×10^{-2}	8.22×10^{-5}	6.90×10^{-8}	-7.71	-9.48	-4.64	-5.55	-11.06	-21.32
	150	14	2.01	-29.15	1.09×10^{-2}	5.80×10^{-5}	7.33×10^{-8}	-7.68	-9.45	-4.79	-5.70	-11.21	-21.47
	150	14	2.01	-29.45	1.09×10^{-2}	5.59×10^{-5}	3.83×10^{-8}	-7.96	-9.74	-4.81	-5.71	-11.23	-21.49
	200	14	2.02	-30.76	1.09×10^{-2}	7.16×10^{-5}	1.72×10^{-8}	-8.42	-9.22	-4.67	-5.93	-11.77	-22.33
	200	14	2.02	-30.83	1.09×10^{-2}	7.44×10^{-5}	1.40×10^{-8}	-8.51	-9.31	-4.66	-5.91	-11.76	-22.31
	200	14	2.02	-31.14	1.09×10^{-2}	7.46×10^{-5}	6.81×10^{-9}	-8.83	-9.62	-4.66	-5.91	-11.76	-22.31
	200	14	2.03	-30.88	1.07×10^{-2}	5.45×10^{-5}	1.57×10^{-8}	-8.46	-9.24	-4.79	-6.04	-11.87	-22.42
	200	14	2.03	-30.89	1.07×10^{-2}	5.60×10^{-5}	1.51×10^{-8}	-8.48	-9.26	-4.78	-6.02	-11.86	-22.41
	250	14	2.03	-33.16	1.09×10^{-2}	6.37×10^{-5}	2.47×10^{-9}	-9.51	-9.48	-4.71	-6.37	-12.66	-23.65
	250	14	2.03	-33.15	1.09×10^{-2}	6.29×10^{-5}	2.55×10^{-9}	-9.49	-9.47	-4.71	-6.38	-12.66	-23.66

Type	t (°C)	Time (days)	pH$_T$	logQ_{s0}	$m_{\mathrm{ClO_4^-}}$	m_{P}	m_{REE}	log$a_{\mathrm{REE^{3+}}}$	log$a_{\mathrm{REEOH^{2+}}}$	log$a_{\mathrm{H_3PO_4}}$	log$a_{\mathrm{H_2PO_4^-}}$	log$a_{\mathrm{HPO_4^{2-}}}$	log$a_{\mathrm{PO_4^{3-}}}$
TmPO$_4$	100	14	2.02	-28.91	1.07×10^{-2}	6.30×10^{-5}	2.14×10^{-8}	-8.14	-11.12	-4.81	-5.39	-10.66	-20.76
	100	14	2.02	-29.10	1.07×10^{-2}	6.10×10^{-5}	1.41×10^{-8}	-8.32	-11.30	-4.83	-5.41	-10.68	-20.78
	100	14	2.02	-28.97	1.07×10^{-2}	5.09×10^{-5}	2.28×10^{-8}	-8.11	-11.09	-4.91	-5.48	-10.75	-20.86
	100	14	2.02	-28.68	1.07×10^{-2}	4.96×10^{-5}	4.61×10^{-8}	-7.81	-10.79	-4.92	-5.49	-10.77	-20.87
	150	16	2.01	-29.31	1.09×10^{-2}	7.40×10^{-5}	3.98×10^{-8}	-7.94	-9.68	-4.69	-5.59	-11.11	-21.37
	150	16	2.01	-29.17	1.09×10^{-2}	7.48×10^{-5}	5.46×10^{-8}	-7.81	-9.55	-4.68	-5.59	-11.10	-21.36
	150	16	2.01	-29.65	1.09×10^{-2}	7.57×10^{-5}	1.77×10^{-8}	-8.30	-10.03	-4.68	-5.58	-11.10	-21.36
	150	14	2.01	-29.50	1.09×10^{-2}	5.91×10^{-5}	3.25×10^{-8}	-8.03	-9.77	-4.79	-5.69	-11.20	-21.46
	150	14	2.01	-29.72	1.09×10^{-2}	6.12×10^{-5}	1.88×10^{-8}	-8.27	-10.01	-4.77	-5.68	-11.19	-21.45
	200	14	2.02	-31.19	1.09×10^{-2}	5.13×10^{-5}	8.99×10^{-9}	-8.71	-9.45	-4.82	-6.07	-11.92	-22.48
	200	14	2.02	-30.93	1.09×10^{-2}	7.34×10^{-5}	1.12×10^{-8}	-8.61	-9.36	-4.66	-5.92	-11.76	-22.32
	200	14	2.02	-31.11	1.09×10^{-2}	7.67×10^{-5}	7.23×10^{-9}	-8.80	-9.54	-4.64	-5.90	-11.74	-22.30
	200	14	2.03	-31.12	1.07×10^{-2}	6.03×10^{-5}	8.27×10^{-9}	-8.74	-9.47	-4.75	-5.99	-11.83	-22.38
	200	14	2.03	-30.95	1.07×10^{-2}	5.35×10^{-5}	1.38×10^{-8}	-8.52	-9.25	-4.80	-6.04	-11.88	-22.43
	250	14	2.03	-33.28	1.09×10^{-2}	4.74×10^{-5}	2.67×10^{-9}	-9.49	-9.40	-4.84	-6.50	-12.79	-23.78
	250	14	2.03	-33.49	1.09×10^{-2}	6.45×10^{-5}	1.20×10^{-9}	-9.84	-9.75	-4.70	-6.37	-12.65	-23.65
LuPO$_4$	100	14	2.02	-29.38	1.07×10^{-2}	4.66×10^{-5}	9.66×10^{-9}	-8.49	-11.45	-4.95	-5.52	-10.79	-20.89
	100	14	2.02	-29.24	1.07×10^{-2}	5.86×10^{-5}	1.07×10^{-8}	-8.44	-11.41	-4.85	-5.42	-10.69	-20.79

Type	t (°C)	Time (days)	pH$_T$	logQ_{s0}	$m_{ClO_4^-}$	m_P	m_{REE}	log$a_{REE^{3+}}$	log$a_{REEOH^{2+}}$	log$a_{H_3PO_4}$	log$a_{H_2PO_4^-}$	log$a_{HPO_4^{2-}}$	log$a_{PO_4^{3-}}$
	150	16	2.01	-29.89	1.09×10^{-2}	7.59×10^{-5}	1.02×10^{-8}	-8.53	-10.27	-4.68	-5.58	-11.09	-21.35
	150	16	2.01	-29.87	1.09×10^{-2}	7.68×10^{-5}	1.05×10^{-8}	-8.52	-10.26	-4.67	-5.58	-11.09	-21.35
	150	16	2.01	-29.54	1.09×10^{-2}	7.38×10^{-5}	2.34×10^{-8}	-8.18	-9.91	-4.69	-5.59	-11.11	-21.37
	150	14	2.01	-30.42	1.09×10^{-2}	6.07×10^{-5}	3.76×10^{-9}	-8.97	-10.70	-4.78	-5.68	-11.19	-21.45
	150	14	2.01	-30.39	1.09×10^{-2}	5.76×10^{-5}	4.29×10^{-9}	-8.91	-10.65	-4.80	-5.70	-11.21	-21.47
	200	14	2.02	-31.34	1.09×10^{-2}	5.20×10^{-5}	6.17×10^{-9}	-8.87	-9.61	-4.81	-6.07	-11.91	-22.47
	200	14	2.02	-31.31	1.09×10^{-2}	5.40×10^{-5}	6.42×10^{-9}	-8.86	-9.59	-4.80	-6.05	-11.90	-22.45
	200	14	2.03	-31.68	1.07×10^{-2}	4.90×10^{-5}	2.79×10^{-9}	-9.21	-9.94	-4.84	-6.08	-11.92	-22.47
	200	14	2.03	-31.35	1.07×10^{-2}	5.91×10^{-5}	4.92×10^{-9}	-8.97	-9.69	-4.76	-6.00	-11.84	-22.39
	250	14	2.03	-34.18	1.09×10^{-2}	5.62×10^{-5}	2.83×10^{-10}	-10.47	-10.37	-4.76	-6.43	-12.71	-23.71
	250	14	2.03	-34.06	1.09×10^{-2}	6.66×10^{-5}	3.18×10^{-10}	-10.42	-10.32	-4.69	-6.35	-12.64	-23.63

Appendix B. Thermodynamic relations.

The relations between the solubility product (K_{s0}), the standard enthalpy of reaction ($\Delta_r H^0$) and isobaric heat capacity ($\Delta \mathrm{C}_P^0$) were determined from van't Hoff's and Kirchhoff's equations,

$$\frac{\delta ln K_{\mathrm{s0}}}{\delta T} = \frac{\Delta_r H_T^0}{RT^2} \tag{B.1}$$

$$(\frac{\delta \Delta H^0}{\delta T})_P = \Delta C_P^0 \tag{B.2}$$

the symbol R is the ideal gas constant ($J\ mol^{-1} K^{-1}$) and T the temperature in Kelvin (K). The heat capacity (C_P^0 in $J\ mol^{-1} K^{-1}$) is represented by the Haas and Fisher (1976) equation,

$$\Delta C_P^0 = a_0 + a_1 T + a_2 T^{-2} + a_3 T^{-0.5} + a_4 T^2 \tag{B.3}$$

Integration of the C_P equation from the reference temperature T_r to temperature T yields enthalpy,

$$\int_{T_r}^{T} \Delta C_P^0 dT = \Delta_r H_T^0 - \Delta_r H_{T_r}^0 \tag{B.4}$$

$$\Delta_r H_T^0 = h_{Tr} + a_0 T + \frac{a_1}{2} T^2 - \frac{a_2}{T} + 2a_3 T^{0.5} + \frac{a_4}{3} T^3 \tag{B.5}$$

where h_{Tr} is a constant enthalpy term according to,

$$h_{Tr} = \Delta_r H_{T_r}^0 - a_0 T_r - \frac{a_1}{2} T_r^2 + \frac{a_2}{T_r} - 2a_3 T_r^{0.5} - \frac{a_4}{3} T_r^3 \tag{B.6}$$

The following integration of the C_P equation allows determining the standard entropy of reaction ($\Delta_r S^0$),

$$\int_{T_r}^{T} \frac{\Delta C_P^0}{T} dT = \Delta_r S_T^0 - \Delta_r S_{T_r}^0 \tag{B.7}$$

with the definition of a constant entropy term (s_{Tr}) according to,

$$s_{Tr} = \Delta_r S_{T_r}^0 - a_0 ln T_r - \frac{a_1}{T}_r + \frac{a_2}{2T_r^2} + 2a_3 T_r^{-0.5} - \frac{a_4}{2} T_r^2 \tag{B.8}$$

Integration of the Van't Hoff's equation (Eq. B.1) permits relating the fitted coefficients of Equation 14 ($A - D$) to the standard entropy and enthalpy of reaction at reference temperature. For a four parameters equation ($A_0 - A_3$),

$$lnK_{s0} = A_0 + A_1 T + A_2/T + A_3 ln(T) \tag{B.9}$$

the following relations can be derived,

$A_0 = Aln(10) = (s_{T_r} - a_0)/R$

$A_1 = Bln(10) = a_1/(2R)$

$A_2 = Cln(10) = -h_{T_r}/R$

$A_3 = Dln(10) = a_0/R$

References

Andersen, A.K., Clark, J.G., Larson, P.B., Donovan, J.J., 2017. REE fractionation, mineral speciation, and supergene enrichment of the Bear Lodge carbonatites, Wyoming, USA. Ore Geology Reviews 89, 780–807.

Andersen, A.K., Clark, J.G., Larson, P.B., Neill, O.K., 2016. Mineral chemistry and petrogenesis of a HFSE(+HREE) occurrence, peripheral to carbonatites of the Bear Lodge alkaline complex, Wyoming. American Mineralogist 101, 1604–1623.

Andersen, A.K., Larson, P.B., Cosca, M.A., 2019. C−O stable isotope geochemistry and 40Ar/39Ar geochronology of the Bear Lodge carbonatite stockwork Wyoming, USA. Lithos 324-325, 640–660.

Andrehs, G., Heinrich, W., 1998. Experimental determination of REE distributions between monazite and xenotime: potential for temperature-calibrated geochronology. Chemical Geology 149, 83–96.

Aries, S., Valladon, M., Polvé, M., Dupré, B., 2000. A routine method for oxide and hydroxide interference corrections in ICP-MS chemical analysis of environmental and geological samples. Geostandards Newsletter 24, 19–31.

Arinicheva, Y., Gausse, C., Neumeier, S., Brandt, F., Rozov, K., Szenknect, S., Dacheux, N., Bosbach, D., Deissmann, G., 2018. Influence of temperature on the dissolution kinetics of synthetic $LaPO_4$-monazite in acidic media between 50 and 130 °C. Journal of Nuclear Materials 509, 488–495.

Bodeving, S., Williams-Jones, A.E., Swinden, S., 2017. Carbonate – silicate melt immiscibility, REE mineralising fluids, and the evolution of the Lofdal Intrusive Suite, Namibia. Lithos 268, 383–398.

Byrne, R.H., Kim, K.H., 1993. Rare earth precipitation and coprecipitation behavior: The limiting role of PO_4^{3-} on dissolved rare earth concentrations in seawater. Geochimica et Cosmochimica Acta 57, 519–526.

Cetiner, Z.S., Wood, S.A., Gammons, C.H., 2005. The aqueous geochemistry of rare earth elements. Part XIV. The solubility of rare earth element phosphates from 23 to 150 °C. Chemical Geology 217, 147–169.

Cherniak, D., Pyle, J., Rakovan, J., 2004. Synthesis of REE and Y phosphates by Pb-free flux methods and their utilization as standards for electron microprobe analysis and in design of monazite chemical U-Th-Pb dating protocol. American Mineralogist 89, 1533–1539.

Cook, N.J., Ciobanu, C.L., O'Rielly, D., Wilson, R., Das, K., Wade, B., 2013. Mineral chemistry of Rare Earth Element (REE) mineralization, Browns Ranges, Western Australia. Lithos 172-173, 192–213.

Du Fou de Kerdaniel, E., Clavier, N., Dacheux, N., Terra, O., Podor, R., 2007. Actinide solubility-controlling phases during the dissolution of phosphate ceramics. Journal of Nuclear Materials 362, 451–458.

England, G.L., Rasmussen, B., McNaughton, N.J., Fletcher, I.R., Groves, D.I., Krapez, B., 2002. SHRIMP U−Pb ages of diagenetic and hydrothermal xenotime from the Archaean Witwatersrand Supergroup of South Africa. Terra Nova 13, 360–367.

Firsching, F., Brune, S., 1991. Solubility products of the trivalent rare-earth phosphates. Journal of Chemical and Engineering Data 36, 93–95.

Gausse, C., Szenknect, S., Qin, D.W., Mesbah, A., Clavier, N., Neumeier, S., Bosbach, D., Dacheux, N., 2016. Determination of the solubility of rhabdophanes $LnPO_4 \cdot 0.667H_2O$ (Ln = La to Dy). European Journal of Inorganic Chemistry 2016, 4615–4630.

Gavrichev, K., Ryumin, M., Khoroshilov, A., Nikiforova, G., Tyurin, A., Gurevich, V., Starykh, R., 2013. Thermodynamic properties and phase transitions of tetragonal modification of terbium orthophosphate. Vestnik (Herald) of St. Petersburg State University 4, 186–197 (in Russian).

Gavrichev, K., Smirnova, N., Gurevich, V., Danilov, V., Tyurin, A., Ryumin, M., Komissarova, L., 2006. Heat capacity and thermodynamic functions of $LuPO_4$ in the range $0-320$ K. Thermochimica Acta 448, 63–65.

Geisler, T., Popa, K., Konings, R.J.M., 2016. Evidence for lattice strain and non-ideal behavior in the $(La_{1-x}Eu_x)PO_4$ solid solution from X-ray diffraction and vibrational spectroscopy. Frontiers in Earth Science 4, 1–12.

Gratz, R., Heinrich, W., 1997. Monazite-xenotime thermobarometry: Experimental calibration of the miscibility gap in the binary system $CePO_4$-YPO_4. American Mineralogist 82, 772–780.

Gratz, R., Heinrich, W., 1998. Monazite-xenotime thermobarometry. III. Experimental calibration of the partitioning of gadolinium between monazite and xenotime. European Journal of Mineralogy 10, 579–588.

Guan, Q., Mei, Y., Etschmann, B., Testemale, D., Louvel, M., Brugger, J., 2020. Yttrium complexation and hydration in chloride-rich hydrothermal fluids: A combined ab initio molecular dynamics and in situ X-ray absorption spectroscopy study. Geochimica et Cosmochimica Acta 281, 168–189.

Gysi, A.P., 2017. Numerical simulations of CO_2 sequestration in basaltic rock formations: Challenges for optimizing mineral-fluid reactions. Pure and Applied Chemistry 89, 581–596.

Gysi, A.P., Harlov, D., Miron, G.D., 2018. The solubility of monazite ($CePO_4$), $SmPO_4$, and $GdPO_4$ in aqueous solutions from 100 to 250 °C. Geochimica et Cosmochimica Acta 242, 143–164.

Gysi, A.P., Williams-Jones, A.E., 2013. Hydrothermal mobilization of pegmatite-hosted REE and Zr at Strange Lake Canada: A reaction path model. Geochimica et Cosmochimica Acta 122, 324–352.

Gysi, A.P., Williams-Jones, A.E., Harlov, D.E., 2015. The solubility of xenotime-(Y) and other HREE phosphates ($DyPO_4$, $ErPO_4$ and $YbPO_4$ in aqueous solutions from 100 to 250 °C and p_{sat}. Chemical Geology 401, 83–95.

Haas, J.L., Fisher, J.R., 1976. Simultaneous evaluation and correlation of thermodynamic data. Am. J. Sci. 276, 525–545.

Haas, J.R., Shock, E.L., Sassani, D.C., 1995. Rare earth elements in hydrothermal systems: Estimates of standard partial molal thermodynamic properties of aqueous complexes of the rare earth elements at high pressures and temperatures. Geochimica et Cosmochimica Acta 59, 4329–4350.

Harlov, D.E., Meighan, C.J., Kerr, I.D., Samson, I.M., 2016. Mineralogy, chemistry, and fluid-aided evolution of the Pea Ridge Fe Oxide-(Y + REE) deposit, Southeast Missouri, USA. Economic Geology 111, 1963–1984.

Heinrich, W., Andrehs, G., Franz, G., 1997. Monazite–xenotime miscibility gap thermometry. I. An empirical calibration. Journal of Metamorphic Geology 15, 3–16.

Helgeson, H.C., Kirkham, D.H., Flowers, G.C., 1981. Theoretical prediction of the thermodynamic behavior of aqueous electrolytes by high pressures and temperatures: IV. Calculation of activity coefficients osmotic coefficients, and apparent molal and standard and relative partial molal properties to 600 °C and 5kb. American Journal of Science 281, 1249–1516.

Hetherington, C., Jercinovic, M., Williams, M., Mahan, K., 2008. Understanding geologic processes with xenotime: Composition, chronology, and a protocol for electron probe microanalysis. Chemical Geology 254, 133–147.

Hirsch, A., Kegler, P., Alencar, I., Ruiz-Fuertes, J., Shelyug, A., Peters, L., Schreinemachers, C., Neumann, A., Neumeier, S., Liermann, H.P., Navrotsky, A., Roth, G., 2017. Structural, vibrational, and thermochemical properties of the monazite-type solid solution $\mathrm{La}_{1-x}\mathrm{Pr}_x\mathrm{PO}_4$. Journal of Solid State Chemistry 245, 82–88.

Hofstra, A.H., Meighan, C.J., Song, X., Samson, I., Marsh, E.E., Lowers, H.A., Emsbo, P., Hunt, A.G., 2016. Mineral thermometry and fluid inclusion studies of the Pea Ridge iron oxide-apatite-rare earth element deposit, Mesoproterozoic St. Francois Mountains Terrane, Southeast Missouri, USA. Economic Geology 111, 1985–2016.

Ji, Y., Beridze, G., Bosbach, D., Kowalski, P.M., 2017. Heat capacities of xenotime-type ceramics: An accurate ab initio prediction. Journal of Nuclear Materials 494, 172–181.

Johnson, J.W., Oelkers, E.H., Helgeson, H.C., 1992. SUPCRT92: A software package for calculating the standard molal thermodynamic properties of minerals gases, aqueous species, and reactions from 1 to 5000 bar and 0 to 1000 °C. Computers & Geosciences 18, 899–947.

Jonasson, R.G., Bancroft, G.M., Nesbitt, H.W., 1985. Solubilities of some hydrous REE phosphates with implications for diagenesis and sea water concentrations. Geochimica et Cosmochimica Acta 49, 2133–2139.

Kestin, J., Sengers, J., Kamgar-Parsi, B., Levelt Sengers, J., 1984. Thermophysical properties of fluid H_2O. Journal of Physical and Chemical Reference data 13, 175–183.

Kielland, J., 1937. Individual activity coefficients of ions in aqueous solutions. Journal of the American Chemical Society 59, 1675–1678.

Kulik, D.A., Wagner, T., Dmytrieva, S.V., Kosakowski, G., Hingerl, F.F., Chudnenko, K.V., Berner, U.R., 2013. GEM-Selektor geochemical modeling package: Revised algorithm and GEMS3K numerical kernel for coupled simulation codes. Computational Geosciences 17, 1–24.

Li, Y., Kowalski, P.M., Blanca-Romero, A., Vinograd, V., Bosbach, D., 2014.

Ab initio calculation of excess properties of $La_{1-x}(Ln,An)_xPO_4$ solid solutions. Journal of Solid State Chemistry 220, 137–141.

Liu, X., Byrne, R.H., 1997. Rare earth and yttrium phosphate solubilities in aqueous solution. Geochimica et Cosmochimica Acta 61, 1625–1633.

Louvel, M., Bordage, A., Testemale, D., Zhou, L., Mavrogenes, J., 2015. Hydrothermal controls on the genesis of REE deposits: Insights from an in situ XAS study of Yb solubility and speciation in high temperature fluids. Chemical Geology 417, 228–237.

Mair, P., Tropper, P., Harlov, D.E., Manning, C.E., 2017. The solubility of $CePO_4$ monazite and YPO_4 xenotime in KCl-H_2O fluids at 800 °C and 1.0 GPa: Implications for REE transport in high-grade crustal fluids. American Mineralogist 102, 2457–2466.

McDonough, W.F., Sun, S., 1995. The composition of the Earth. Chemical Geology 120, 223–253.

McNaughton, N.J., Rasmussen, B., 2018. Geochemical characterisation of xenotime formation environments using U−Th. Chemical Geology 484, 109–119.

Mercer, C.N., Watts, K.E., Gross, J., 2020. Apatite trace element geochemistry and cathodoluminescent textures – A comparison between regional magmatism and the Pea Ridge IOAREE and Boss IOCG deposits, southeastern Missouri iron metallogenic province, USA. Ore Geology Reviews 116, 1–22.

Mesbah, A., Clavier, N., Elkaim, E., Szenknect, S., Dacheux, N., 2017. In pursuit of the rhabdophane crystal structure: From the hydrated monoclinic $LnPO_4 \cdot 0.667H_2O$ to the hexagonal $LnPO_4$(Ln = Nd, Sm, Gd, Eu and Dy). Journal of Solid State Chemistry 249, 221–227.

Migdisov, A.A., Guo, X., Nisbet, H., Xu, H., Williams-Jones, A.E., 2019. Fractionation of REE, U, and Th in natural ore-forming hydrothermal systems: Thermodynamic modeling. Journal of Chemical Thermodynamics 128, 305–319.

Migdisov, A.A., Williams-Jones, A.E., 2007. An experimental study of the solubility and speciation of neodymium (III) fluoride in F-bearing aqueous solutions. Geochimica et Cosmochimica Acta 71, 3056–3069.

Migdisov, A.A., Williams-Jones, A.E., 2014. Hydrothermal transport and deposition of the rare earth elements by fluorine-bearing aqueous liquids. Mineralium Deposita 49, 987–997.

Migdisov, A.A., Williams-Jones, A.E., Brugger, J., Caporuscio, F.A., 2016. Hydrothermal transport deposition, and fractionation of the REE: Experimental data and thermodynamic calculations. Chemical Geology 439, 13–42.

Migdisov, A.A., Williams-Jones, A.E., Wagner, T., 2009. An experimental study of the solubility and speciation of the Rare Earth Elements (III) in fluoride- and chloride-bearing aqueous solutions at temperatures up to 300 °C. Geochimica et Cosmochimica Acta 73, 7087–7109.

Miron, G.D., Kulik, D.A., Dmytrieva, S.V., Wagner, T., 2015. GEMSFITS: Code package for optimization of geochemical model parameters and inverse modeling. Applied Geochemistry 55, 28–45.

Navrotsky, A., Lee, W., Mielewczyk-Gryn, A., Ushakov, S.V., Anderko, A., Wu, H., Riman, R.E., 2015. Thermodynamics of solid phases containing rare earth oxides. Journal of Chemical Thermodynamics 88, 126–141.

Neumeier, S., Kegler, P., Arinicheva, Y., Shelyug, A., Kowalski, P.M., Schreinemachers, C., Navrotsky, A., Bosbach, D., 2017. Thermochemistry of $La_{1-x}Ln_xPO_4$-monazites (Ln = Gd, Eu). Journal of Chemical Thermodynamics 105, 396–403.

Ni, Y., Hughes, J.M., Mariano, A.N., 1995. Crystal chemistry of the monazite and xenotime structures. American Mineralogist 80, 21–26.

Nikiforova, G., Ryumin, M., Gavrichev, K., Gurevich, V., 2012. High-temperature thermodynamic properties of $LuPO_4$. Inorganic Materials 48, 841–844.

Ochiai, A., Utsunomiya, S., 2017. Crystal chemistry and stability of hydrated rare-earth phosphates formed at room temperature. Minerals 7, 1–22.

Perry, E.P., Gysi, A.P., 2018. Rare earth elements in mineral deposits: Speciation in hydrothermal fluids and partitioning in calcite. Geofluids 2018, 1–19.

Poitrasson, F., Hanchar, J.M., Schaltegger, U., 2002. The current state and future of accessory mineral research. Chemical geology 191, 3–24.

Popa, K., Konings, R., Geisler, T., 2007. High-temperature calorimetry of $(La_{1-x}Ln_x)PO_4$ solid solutions. Journal of Chemical Thermodynamics 39, 236–239.

Pourtier, E., Devidal, J.L., Gibert, F., 2010. Solubility measurements of synthetic neodymium monazite as a function of temperature at 2 kbars, and aqueous neodymium speciation in equilibrium with monazite. Geochimica et Cosmochimica Acta 74, 1872–1891.

Rasmussen, B., Fletcher, I.R., Muhling, J.R., Gregory, C.J., Wilde, S.A., 2011. Metamorphic replacement of mineral inclusions in detrital zircon from Jack Hills, Australia: Implications for the Hadean Earth. Geology 39, 1143–1146.

Rasmussen, B., Fletcher, I.R., Muhling, J.R., Thorne, W.S., Broadbent, G.C., 2007. Prolonged history of episodic fluid flow in giant hematite ore bodies: Evidence from in situ U−Pb geochronology of hydrothermal xenotime. Earth and Planetary Science Letters 258, 249–259.

Richter, L., Diamond, L.W., Atanasova, P., Banks, D.A., Gutzmer, J., 2018. Hydrothermal formation of heavy rare earth element (HREE)–xenotime deposits at 100 °C in a sedimentary basin. Geology 46, 263–266.

Robinson, R.A., Stokes, R.M., 1968. Electrolyte solutions. Butterworths, London .

Shannon, R.D., 1976. Revised effective ionic radii and systematic studies of interatomic distances in halides and chalcogenides. Acta Crystallographica A 32, 751–767.

Shelyug, A., Mesbah, A., Szenknect, S., Clavier, N., Dacheux, N., Navrotsky, A., 2018. Thermodynamics and stability of rhabdophanes, hydrated rare earth phosphates $REPO_4 \cdot n\ H_2O$. Frontiers in Chemistry 6, 1–11.

Shock, E., Sassani, D., Willis, M., Sverjensky, D., 1997. Inorganic species in geologic fluids: correlations among standard molal thermodynamic properties of aqueous ions and hydroxide complexes. Geochimica et Cosmochimica 61, 907–950.

Shock, E.L., Helgeson, H.C., 1988. Calculation of the thermodynamic and transport properties of aqueous species at high pressures and temperatures: Correlation algorithms for ionic species and equation of state predictions to 5 kb and 1000 °C. Geochimica et Cosmochimica Acta 52, 2009–2036.

Shock, E.L., Helgeson, H.C., Sverjensky, D.A., 1989. Calculation of the thermodynamic and transport properties of aqueous species at high pressures and temperatures: Standard partial molal properties of inorganic neutral species. Geochimica et Cosmochimica Acta 53, 2157–2183.

Shock, E.L., Oelkers, E.H., Johnson, J.W., Sverjensky, D.A., Helgeson, H.C., 1992. Calculation of the thermodynamic properties of aqueous species at high pressures and temperatures. Effective electrostatic radii dissociation constants and standard partial molal properties to 1000 °C and 5 kbar. Journal of the Chemical Society, Faraday Transactions 88, 803–826.

Subramani, T., Rafiuddin, M.R., Shelyug, A., Ushakov, S., Mesbah, A., Clavier, N., Qin, D., Szenknect, S., Elkaim, E., Dacheux, N., Navrotsky, A., 2019. Synthesis, crystal structure, and enthalpies of formation of churchite-type $REPO_4{\cdot}2H_2O$ (RE = Gd to Lu) Materials. Crystal Growth and Design 19, 4641–4649.

Tanger, J.C., Helgeson, H.C., 1988. Calculation of the thermodynamic and transport properties of aqueous species at high pressures and temperatures: Revised equations of state for the standard partial molal properties of ions and electrolytes. American Journal of Science 288, 19–98.

Tanis, E.A., Simon, A., Tschauner, O., Chow, P., Xiao, Y., Shen, G., Hanchar, J.M., Frank, M., 2012. Solubility of xenotime in a 2 M HCl aqueous fluid from 1.2 to 2.6 GPa and 300 to 500 °C. American Mineralogist 97, 1708–1713.

Tropper, P., Manning, C.E., Harlov, D.E., 2011. Solubility of $CePO_4$ monazite and YPO_4 xenotime in H_2O and H_2O–NaCl at 800 °C and 1GPa: Implications for REE and Y transport during high-grade metamorphism. Chemical Geology 282, 58–66.

Tropper, P., Manning, C.E., Harlov, D.E., 2013. Experimental determination of $CePO_4$ and YPO_4 solubilities in H_2O-NaF at 800 °C and 1 GPa: Implications for rare earth element transport in high-grade metamorphic fluids. Geofluids 13, 372–380.

Tyurin, A., Ryumin, M., Khoroshilov, A., Gurevich, V., Gavrichev, K., 2020. Thermodynamic functions of holmium orthophosphate $HoPO_4$ in the range 9−1370 K. Thermochimica Acta 683, 1–6.

Ushakov, S.V., Helean, K.B., Navrotsky, A., Boatner, L.A., 2001. Thermochemistry of rare-earth orthophosphates. Journal of Materials Research 16, 2623–2633.

Van Hoozen, C.J., Gysi, A.P., Harlov, D.E., 2020. The solubility of monazite ($LaPO_4$, $PrPO_4$, $NdPO_4$, and $EuPO_4$) endmembers in aqueous solutions from 100 to 250 °C. Geochimica et Cosmochimica Acta 280, 302–316.

Wagner, T., Kulik, D.A., Hingerl, F.F., Dmytrieva, S.V., 2012. GEM-Selektor geochemical modeling package: TSolMod library and data interface for multicomponent phase models. Canadian Mineralogist 50, 1173–1195.

Wall, F., Niku-Paavola, V., Storey, C., Müller, A., Jeffries, T., 2008. Xenotime-(Y) from carbonatite dykes at Lofdal, Namibia: Unusually low LREE:HREE ratio in carbonatite, and the first dating of xenotime overgrowths on zircon. Canadian Mineralogist 46, 861–877.

Wood, S.A., Palmer, D.A., Wesolowski, D.J., Bénézeth, P., 2002. The aqueous geochemistry of the rare earth elements and yttrium. Part XI. The solubility of $Nd(OH)_3$ and hydrolysis of Nd^{3+} from 30 to 290 °C at saturated water vapor pressure with in-situ pH_m measurement. Geochemical Society Special Publication 7, 229–256.

Zhou, L., Mavrogenes, J., Spandler, C., Li, H., 2016. A synthetic fluid inclusion study of the solubility of monazite-(La) and xenotime-(Y) in in H_2O-Na-K-Cl-F-CO_2 fluids at 800 °C and 0.5 GPa. Chemical Geology 442, 121–129.

Zi, J.W., Rasmussen, B., Muhling, J.R., Fletcher, I.R., Thorne, A.M., Johnson, S.P., Cutten, H.N., Dunkley, D.J., Korhonen, F.J., 2015. In situ U−Pb geochronology of xenotime and monazite from the Abra polymetallic deposit in the Capricorn Orogen, Australia: Dating hydrothermal mineralization and fluid flow in a long-lived crustal structure. Precambrian Research 260, 91–112.